

Diplomarbeit

Constrained Capacity Density Optimization by Fractional Frequency Partitioning

Ausgeführt zum Zwecke der Erlangung des akademischen Grades eines
Diplom-Ingenieurs unter Leitung von

Univ.Prof. Dipl.-Ing. Dr.techn. Markus Rupp
Josep Colom Ikuno, M.Sc.

E389
Institute of Telecommunications

eingereicht an der Technischen Universität Wien
Fakultät für Elektrotechnik und Informationstechnik

von

Martin Taranetz

Matrikelnr.: 0525719
Markt 50, 3321 Ardagger Markt, Österreich

Wien, Februar 2011

.....

I certify that the work presented in this diploma thesis was done by myself
and the work of other authors is properly cited.

Martin Taranetz
Vienna, February 2011

Abstract

Downlink performance of cellular networks is mainly limited by Inter-cell Interference (ICI). A promising concept for ICI mitigation is Fractional Frequency Reuse (FFR), which effectively allows to trade off overall performance against enhanced cell-edge performance.

In this work, a novel FFR scheme is proposed. It assigns a given user to a frequency sub band depending on the achievable capacity density ($bit/s/m^2$). An optimization problem is formulated, which aims at maximizing average per-user throughput while maintaining a minimum performance at cell-edge. Simulations are carried out for omnidirectional and sectorized cellular scenarios, using both Two-dimensional (2-D) and Three-dimensional (3-D) antenna radiation patterns. The simulation results show that the proposed scheme outperforms conventional reuse-1- and reuse-3 schemes in terms of average- and cell-edge performance.

Contents

1	Fractional Frequency Reuse Concept and Terms	1
2	System Model	6
3	Reuse-Partitioning Optimization	10
3.1	Optimization Problem	10
3.1.1	General Problem Formulation	10
3.1.2	Reuse-Partitioning Optimization Problem	11
3.2	Assumptions and Simplifications	13
3.2.1	Noise and Interference Limitation	13
3.2.2	Circular Symmetry	13
3.2.3	Bandwidth Density and Capacity Density	14
3.2.4	User Density	16
3.2.5	Definition of Average Capacity Density	16
3.2.6	Average Reuse-Partitioning Capacity Density	17
3.3	Optimization Proposal	18
4	Simulation Results of Omnidirectional Scenarios	21
4.1	Simulation Setup	21
4.2	Calculation Methods	23
4.3	One-Ring Scenario	23
4.4	Noise Power versus Interference Power	25
4.5	Two-Rings Scenario	29
5	Optimization of Reuse Partitioning in Sectorized Scenarios	33
5.1	Introduction and Cell Design	33
5.2	Path Loss and Antenna Radiation Patterns	35
5.2.1	Propagation Path Loss	35
5.2.2	Two-dimensional Antenna Radiation Pattern	36
5.2.3	Three-dimensional Antenna Radiation Pattern	37
5.3	Signal-to-Noise-and-Interference Contours	37
5.4	Optimization of Sectorized Scenarios	41
5.4.1	Optimization Proposal	41
5.4.2	Average Capacity Density	42

6	Simulation Results of Sectorized Scenarios	43
6.1	Simulation Setup and Calculation Methods	43
6.1.1	Assumptions and Simulation Parameters	43
6.1.2	Calculation Methods	45
6.2	Simulation Results of Two-dimensional Scenarios	46
6.3	Simulation Results of Three-dimensional Scenarios	50
6.4	Optimization Results	56
7	Conclusion and Outlook	59
A	Acronyms	61
	Bibliography	61

List of Figures

1.1	Exemplary frequency-reuse partitioning	2
1.2	Cell of radius R with partitioning boundary ρ	3
1.3	Exemplary capacity-density ECDF curves for reuse-1, reuse-3 and FFR	4
2.1	Cellular system with hexagonal cells of radius R [1]	7
2.2	Distances of user $U(X, Y)$ to base stations BS_k	8
3.1	An FFR scheme using reuse-3: (a) Cell cluster (b) Bandwidth partitioning	12
3.2	Exemplary full-reuse Signal-to-Interference-plus-Noise Ratio (SINR)-map with constant-SINR contours	14
3.3	Capacity densities and switching radius ρ , $R = 250$ m	19
3.4	Exhaustive search for mapping $\rho(\beta_{FR})$: $ c_{FR,\rho,\beta_{FR}}(r) - c_{PR,\rho,\beta_{PR}}(r) $	20
4.1	One-ring scenario with sector assignment. Full Reuse (FR) zone depicted in blue. Partial Reuse (PR) zones depicting the employed reuse-3 scheme	24
4.2	Mapping $\rho(\beta_{FR})$ in one-ring scenario	24
4.3	(a) Average capacity densities in one-ring scenario. FFR de- picted in blue. Red and green lines depict reuse-1- and reuse-3 average per-user capacities respectively. (b) Bandwidth allo- cation of FFR, reuse-1 and reuse-3	25
4.4	Two-rings scenario with sector assignment. FR zone depicted in blue. PR zones depicting the employed FRF = 3.	26

4.5	Comparison of signal- and noise power density (a) reuse-1: $p_{\text{CCI,FRF1}}(x, y)/N_0$ (dB), (b) reuse-3: $p_{\text{CCI,FRF3}}(x, y)/N_0$ (dB) .	27
4.6	$p_{\text{CCI,FRF3}}(x, y)/N_0$ (dB) along the horizontal center axis of the cell cluster; $R = 250$ m	28
4.7	$p_{\text{CCI,FRF3}}(x, y)/N_0$ (dB) along the horizontal center axis of the cell cluster; $R = 500$ m	28
4.8	Mapping $\rho(\beta_{\text{FR}})$ in two-rings scenario	30
4.9	(a) Average capacity densities (\bar{c}) and (b) cell-edge capacities ($c_{5\%}$) in two-rings scenario. FFR depicted in blue. Red and green lines depict capacity densities of reuse-1 and reuse-3. Labels denoting points, where FFR achieves no average performance loss compared to reuse-1 ($\beta_{\text{FR}} = 0.52$), reuse-3 equivalent cell-edge performance ($\beta_{\text{FR}} = 0.63$) and maximum average capacity density ($\beta_{\text{FR}} = 0.8$).	30
4.10	(a) Peak capacities ($c_{95\%}$) and (b) peak-to-edge ratio ($c_{95\%}/c_{5\%}$) in two-rings scenario. FFR depicted in blue. Red and green lines depict capacity densities (a) and ratios (b) of reuse-1 and reuse-3.	31
4.11	Empirical Cumulative Distribution Function (ECDF) curves of two-rings scenario at $\beta_{\text{FR}} = 0.8$. In comparison to a reuse-1 scheme, FFR improves for this specific bandwidth allocation $c_{5\%}$ by 32.7% while $c_{95\%}$ is 5.3% higher.	32
4.12	Relative capacity density gains of FFR over conventional reuse-1 scheme in two-rings omnidirectional scenario. Labels denoting points, where FFR achieves no average performance loss compared to reuse-1 ($\beta_{\text{FR}} = 0.52$), reuse-3 equivalent cell-edge performance ($\beta_{\text{FR}} = 0.63$) and maximum average capacity density ($\beta_{\text{FR}} = 0.8$).	32
5.1	(a) Cell design in sectorized scenario (b) SINR map of center site with constant-SINR contours	34
5.2	2-D- and 3-D sectorized scenario	35
5.3	Horizontal antenna radiation pattern referred from [2]	36

5.4	(a) Kathrein 742 215 Panel antenna [3], (b) Horizontal- and vertical radiation pattern plotted in logarithmic scale.	38
5.5	Exemplary channel power gain $L(d) _{\text{dB}}$ using exponential path loss model ($\alpha = 3.6$)	39
5.6	Antenna gain $G_{\text{Tx}}(x, y) _{\text{dB}}$: (a) 2-D (b) 3-D (Antenna electrically downtilted by 8°)	39
5.7	Received power density $p_{\text{Rx}} _{\frac{\text{dBm}}{\text{Hz}}} = p_{\text{Tx}} _{\frac{\text{dBm}}{\text{Hz}}} + G_{\text{Tx}} _{\text{dB}} + L _{\text{dB}}$: (a) 2-D (b) 3-D (Antenna electrically tilted down by 8°) . . .	39
5.8	SINR ECDF curves for 2-D- and 3-D sectorized scenario (antenna electrically downtilted by 8° in 3-D scenario)	40
5.9	SINR map with constant-SINR contours in sectorized scenario: (a) 2-D (b) 3-D (antenna electrically downtilted by 8°)	40
6.1	Cell grid of sectorized scenario. FR zones depicted in blue. PR zones depicting the employed reuse-3 scheme	44
6.2	(a) Cell with three sectors (b) Bandwidth allocation of FFR, reuse-1 and reuse-3	45
6.3	(a) Capacity density switching point: $c_{\text{FR},\rho,\beta_{\text{FR}}}(x, y) = c_{\text{PR},\rho,\beta_{\text{PR}}}(x, y)$ in 2-D sectorized scenario (b) Capacity density map $c_{\text{FR},\rho,\beta_{\text{FR}}}(x, y)$ for $\beta_{\text{FR}} = 0.75$. Partitioning boundary (ρ) depicted as black line.	47
6.4	(a) Average capacity densities, (b) cell-edge capacities and (c) peak capacities in 2-D sectorized scenario. FFR depicted in blue. Red and green lines depicting reuse-1 and reuse-3. Labels denoting points, where FFR achieves no average performance loss compared to reuse-1 ($\beta_{\text{FR}} = 0.40$), reuse-3 equivalent cell-edge performance ($\beta_{\text{FR}} = 0.62$) and maximum average capacity density ($\beta_{\text{FR}} = 0.75$).	48
6.5	Capacity density ECDF curves for $\beta_{\text{FR}} = 0.75$ in 2-D sectorized scenario, FFR depicted in blue. Red and green curves depict reuse-1 and reuse-3 respectively.	49
6.6	Relative capacity density gains of FFR over reuse-1 scheme in 2-D sectorized scenario	50

6.7	Capacity density switching point: $c_{\text{FR},\rho,\beta_{\text{FR}}}(x,y) = c_{\text{PR},\rho,\beta_{\text{FR}}}(x,y)$ in 3-D sectorized scenario	52
6.8	Capacity density map in 3-D sectorized scenario. Black lines depict partitioning boundaries (ρ) at $\beta_{\text{FR}} = 0.75$	52
6.9	(a) Average capacity densities, (b) cell-edge capacities and (c) peak capacities in 3-D sectorized scenario. FFR depicted in blue. Red and green lines depicting reuse-1 and reuse-3. La- bels denoting points, where FFR achieves no average perfor- mance loss compared to reuse-1 ($\beta_{\text{FR}} = 0.40$), reuse-3 equiva- lent cell-edge performance ($\beta_{\text{FR}} = 0.66$) and maximum average capacity density ($\beta_{\text{FR}} = 0.75$).	53
6.10	Relative capacity density gains of FFR over reuse-1 scheme in 3-D sectorized scenario	54
6.11	Capacity-density ECDF for $\beta_{\text{FR}} = 0.75$ in 3-D sectorized sce- nario, FFR depicted in blue. Red and green curves depict reuse-1 and reuse-3 respectively.	55
6.12	Comparison of simulation results for 2-D- and 3-D sectorized scenarios: (a) Relative capacity density gains over reuse-1, (b) average capacity density (bit/s/m^2), (c) cell-edge capacity (bit/s/m^2) and (d) peak capacity(bit/s/m^2)	58
7.1	Simulation results of (a) average capacity densities \bar{c} , (b) edge capacity densities ($c_{5\%}$) and (c) peak capacity densities ($c_{95\%}$) in 2-D-, 3-D- and omnidirectional scenarios	60

List of Tables

4.1	Simulation parameters of omnidirectional scenarios (Cell radius R referred from [4])	22
6.1	Simulation parameters of sectorized scenarios	44
6.2	Relative gains of FFR scheme over reuse-1 at significant bandwidth allocations (β_{FR}) in 2-D sectorized scenario	51
6.3	Relative gains of FFR scheme over reuse-1 at significant bandwidth allocations (β_{FR}) in 3-D sectorized scenario	54

Chapter 1

Fractional Frequency Reuse Concept and Terms

The concept of cellular communication systems dates back to proposals and developments by Bell System in the early 1970's. Since then, frequency reuse has been a key issue for optimizing the use of the scarce spectral resource [1]. A reuse policy must cope with the problem of Inter-cell Interference (ICI). Traditionally, inter-cell interference is handled by classical clustering techniques, of which a cellular network using a Frequency Reuse Factor (FRF) of 3 would be an example. While these Co-Channel Interference (CCI) mitigation techniques reduce interference for the users at the cell edge, they compromise system throughput due to the resource partitioning [5–12]. With a smaller FRF, more available bandwidth can be obtained by each cell. Thus, in this sense a frequency reuse factor of 1 is desirable. However, with the usage of $\text{FRF} = 1$, most users, especially near the cell edge are afflicted with severe ICI.

In order to balance the cell-edge throughput and the overall throughput, Fractional Frequency Reuse (FFR) has been proposed [13–16]. The motivation behind FFR is based on the fact that users in the central area of a cell are more robust against interference due to low path loss and attenuated interference from neighboring sites. Hence, they can tolerate a higher reuse factor compared to those at the cell-edge, which are suffering from high in-

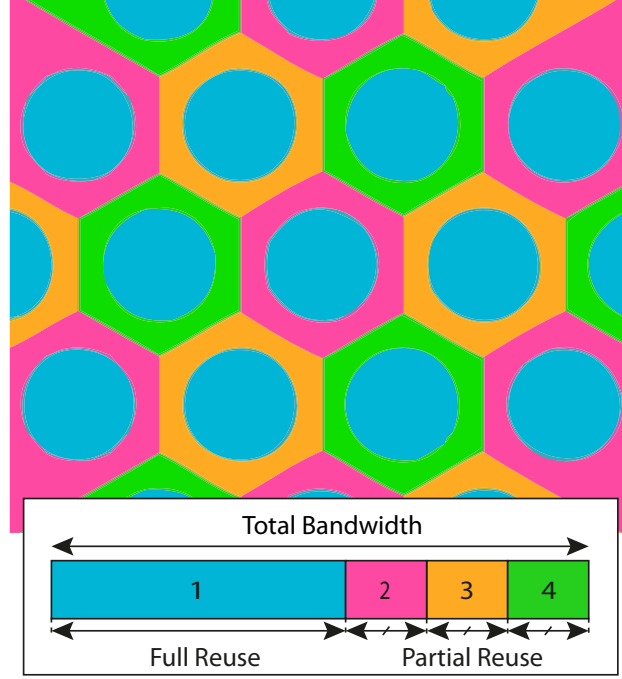


Figure 1.1: Exemplary frequency-reuse partitioning

interference power as well as high path loss. Therefore, the cell is divided into a center zone and an edge zone. In FFR, the frequency spectrum is also split into a center band and an edge band. While the center band is reused by all users in the center zone (Full Reuse (FR) zone), having a low reuse factor, the edge band is further divided and reused by users in the edge zone (Partial Reuse (PR) zone) with a higher order reuse factor. In the literature, $\text{FRF} = 3$ is commonly utilized for the PR zone [6–9, 13, 14, 16, 17], and is used throughout this work. An exemplary reuse partitioning scheme is shown in Figure 1.1.

The boundary between the FR zone and the PR zone is called partitioning boundary (ρ) and is depicted in Figure 1.2.

$\text{FRF} = 1$ (reuse-1) in the FR zone and $\text{FRF} = 3$ (reuse-3) in the PR zone imply different Signal-to-Interference-plus-Noise Ratios (SINRs), which are given in a general form as

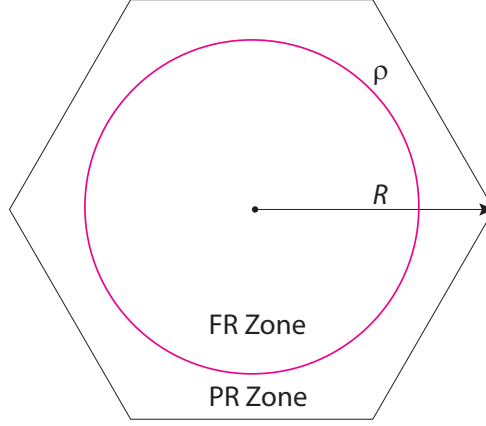


Figure 1.2: Cell of radius R with partitioning boundary ρ

$$\text{SINR} = \frac{p_r}{N_0 + \sum_i p_{i, \text{Co-Channel Interferer}}}, \quad (1.1)$$

where p_r is the received power density (W/Hz) of the wanted signal, $p_{i, \text{Co-Channel Interferer}}$ (W/Hz) is the interference from i -th co-channel interferer and N_0 the noise spectral density (W/Hz). The SINR directly impacts the achievable throughput and thus, the performance of the partitioning scheme. Although throughput is the practical measure, channel capacity as a theoretical valid upper bound serves as performance metric in this work and allows for more convenient mathematical expressions. The well-known channel capacity C in Bits per Second (bit/s) is given as [18]

$$C = B \log_2 (1 + \text{SINR}), \quad (1.2)$$

where B denotes the bandwidth.

In this work, the achievable per-user capacity (bit/s/User) is investigated. For its analysis, the concept of per-area capacity (bit/s/Unit of Surface) will be introduced. With the assumption of constant user density, both concepts are equivalent¹. The per-area capacity is denoted as capacity density and is analogous to the per-user performance throughout this work.

¹see Section 3.2.3

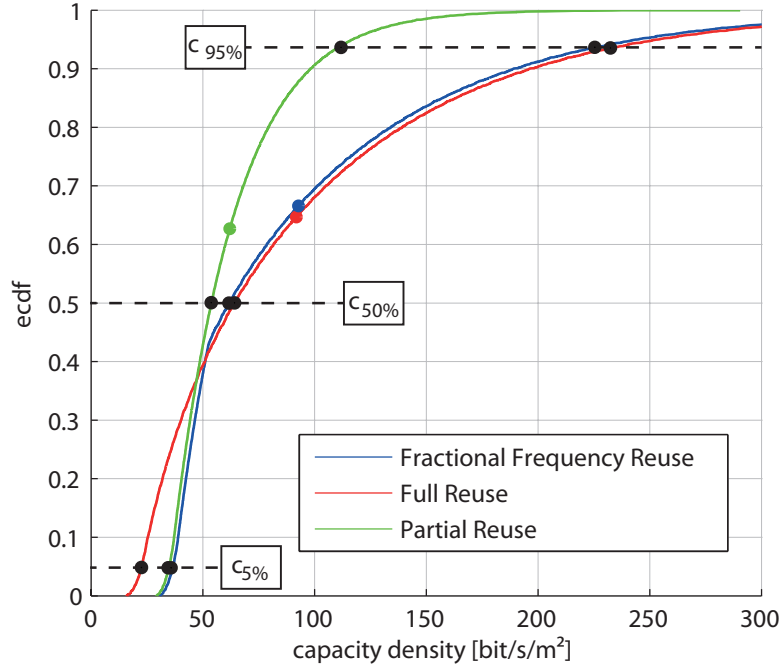


Figure 1.3: Exemplary capacity-density ECDF curves for reuse-1, reuse-3 and FFR

The capacity density distribution within a cell can be depicted by an Empirical Cumulative Distribution Function (ECDF). Figure 1.3 shows ECDF curve examples for reuse-1 (red), reuse-3 (green) and an FFR scheme (blue). The red, green and blue dots denote the corresponding average capacity densities.

A coarse characterization of the capacity density distribution can be obtained by three values: the edge capacity density $c_{5\%}$, the median capacity density $c_{50\%}$ and the peak capacity density $c_{95\%}$, expressing the 5%, 50% (median) and 95% points on the ECDF respectively (Figure 1.3). In this work, the edge capacity $c_{5\%}$ and peak capacity $c_{95\%}$ are used as a measure for the cell-edge- and peak performance².

FFR optimization in this work is aimed at maximizing the average capacity density \bar{c} (analogous to the concept of average per-user throughput), while satisfying a minimum required $c_{5\%}$ cell-edge performance (analogous to the

²Note that the term *density* is obviated for the reader's convenience. Throughout the work, the notions *cell-edge capacity* and *peak capacity* therefore refer to the corresponding cell-edge- and peak capacity density (bit/s/Unit of Surface).

concept of ensuring a minimum edge user throughput) and minimizing the $c_{95\%}$ peak performance loss (analogous to the peak user throughput).

The work is organized as follows: Chapter 2 introduces the cellular system model for analysis. Based on this model, Chapter 3 presents the proposed FFR partitioning scheme and formulates a constrained optimization problem. Then, the scheme is investigated by means of simulations and compared to conventional reuse-1- and reuse-3 schemes. First, Chapter 4 analyzes simulation results in non-sectorized scenarios (i.e. using omnidirectional antennas). Then, Chapter 5 derives methods to employ and optimize the scheme also in sectorized scenarios. The obtained simulation results are discussed in Chapter 6. Finally, Chapter 7 concludes the work.

Chapter 2

System Model

For the system model, the commonly used hexagonal grid layout of cells with radius R , as shown in Figure 2.1, is utilized [1, 19]. Each cell contains a Base Station (BS), equipped with an omnidirectional antenna and a total available transmit power of P_{TOT} .

If the central BS is considered, denoted as BS_0 , it can be assumed that most interference is caused by the six direct neighbors $\text{BS}_1, \dots, \text{BS}_6$. Therefore, only this first tier of interferers is taken into account and the reuse-1 SINR in the central cell can be calculated as

$$\gamma(X, Y) = \frac{p_{\text{Rx}, \text{BS}_0}(X, Y)}{N_0 + \sum_{i=1}^6 p_{\text{Rx}, \text{BS}_i}(X, Y)}, \quad (2.1)$$

where $p_{\text{Rx}, \text{BS}_0}(X, Y)$ is the received power density (W/Hz) of the useful signal, N_0 denotes the noise spectral density and $p_{\text{Rx}, \text{BS}_i}(X, Y)$ is the received power density from the neighboring base station BS_i at point (X, Y) (The capitalized coordinates denote absolute values. Later in this section, relative coordinates denoted by lower case letters are introduced).

In this work, the channel power gain between two points separated by a distance r is restricted to the path loss. To model the macroscopic path loss, an exponential path loss model is used [20], expressed as

$$G(r) = \frac{G_0}{r^\alpha}, \quad (2.2)$$

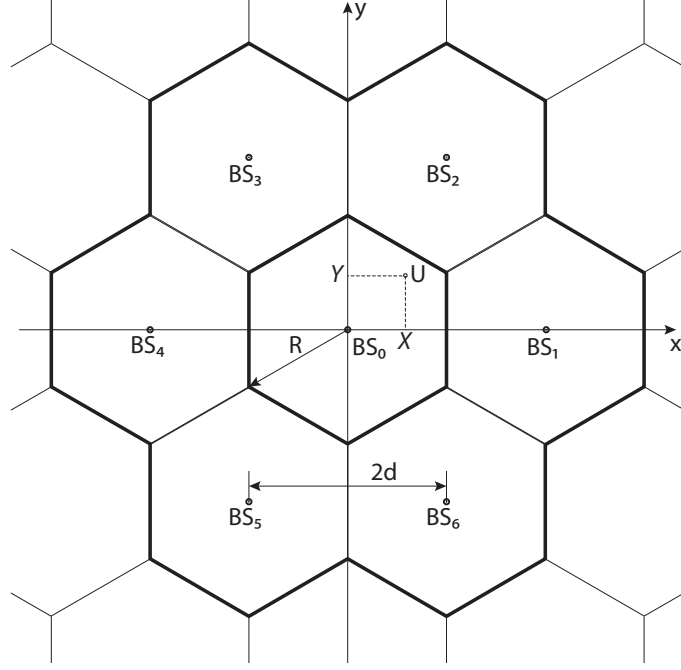


Figure 2.1: Cellular system with hexagonal cells of radius R [1]

where the path loss exponent α includes factors such as antenna height and terrain nature. Typical values of α range from 2 in rural areas to 6 in an urban scenario [21–23]. The constant G_0 is derived from the Friis Transmission Equation as $G_0 = (c_0/(4\pi f_c))^2$, where c_0 denotes the speed of light and f_c the center frequency.

At distance $r = \sqrt{X^2 + Y^2}$, a user $U(X, Y)$ receives a useful signal power density $p_{\text{Rx}, \text{BS}_0}(X, Y) = p_{\text{Tx}} G_0 / r^\alpha$ from BS_0 . With the exponential path loss model, the reuse-1 SINR of Equation (2.1) is thus expressed as

$$\gamma(X, Y) = \frac{p_{\text{Tx}} \frac{G_0}{r^\alpha}}{N_0 + \sum_{i=1}^6 p_{\text{Tx}} \frac{G_0}{r_i^\alpha}}, \quad (2.3)$$

where $r_k = |\overrightarrow{\text{BS}_k U}|$ is the distance of $U(X, Y)$ to BS_k , as depicted in Figure 2.2.

In this work, coordinates (x, y) normalized to the cell radius R will be used, i.e. $(x, y) = (X/R, Y/R)$. Thus, the normalized position of the direct

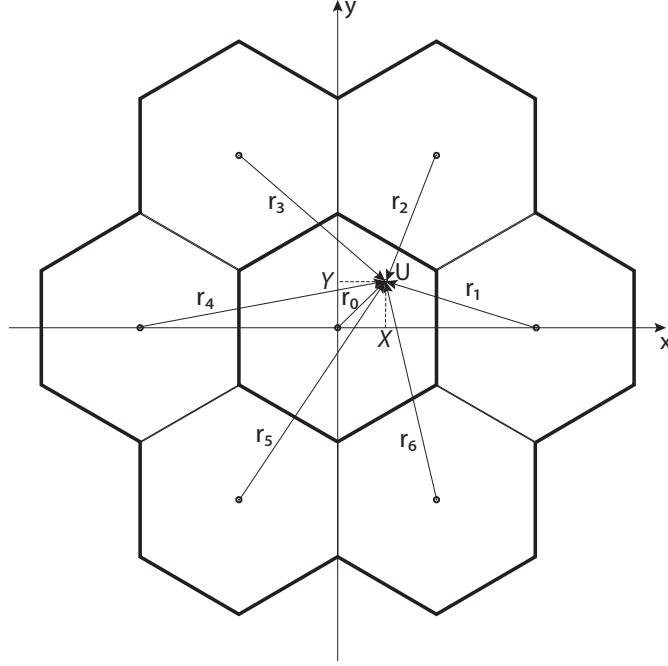


Figure 2.2: Distances of user $U(X, Y)$ to base stations BS_k

neighbor BSs are $BS_1 : (\sqrt{3}, 0)$, $BS_2 : (\sqrt{3}/2, 3/2)$, $BS_3 : (-\sqrt{3}/2, 3/2)$, $BS_4 : (-\sqrt{3}, 0)$, $BS_5 : (-\sqrt{3}/2, -3/2)$ and $BS_6 : (\sqrt{3}/2, -3/2)$. The position of BS_0 coincides with the coordinate origin $(0, 0)$. With normalized coordinates, Equation (2.3) can thus be rewritten as

$$\gamma(x, y) = \frac{\Gamma_e}{(x^2 + y^2)^{\alpha/2} [1 + \Gamma_e S(x, y)]}, \quad (2.4)$$

where

$$\Gamma_e = \frac{p_{Tx} G_0}{N_0 R^\alpha} \quad (2.5)$$

expresses the Signal-to-Noise Ratio (SNR) at the cell-border. The term $S(x, y)$ is a distance measure to the attending interfering BSs, which formulates as:

$$\begin{aligned}
S(x, y) &= \sum_{i=1}^6 ((x - x_{\text{BS},i})^2 + (y - y_{\text{BS},i})^2)^{-\alpha/2} = \tag{2.6} \\
&= \left[(x - \sqrt{3})^2 + y^2 \right]^{-\alpha/2} + \left[(x + \sqrt{3})^2 + y^2 \right]^{-\alpha/2} \\
&+ \left[\left(x - \frac{\sqrt{3}}{2} \right)^2 + \left(y - \frac{3}{2} \right)^2 \right]^{-\alpha/2} \\
&+ \left[\left(x + \frac{\sqrt{3}}{2} \right)^2 + \left(y - \frac{3}{2} \right)^2 \right]^{-\alpha/2} \\
&+ \left[\left(x + \frac{\sqrt{3}}{2} \right)^2 + \left(y + \frac{3}{2} \right)^2 \right]^{-\alpha/2} \\
&+ \left[\left(x - \frac{\sqrt{3}}{2} \right)^2 + \left(y + \frac{3}{2} \right)^2 \right]^{-\alpha/2}.
\end{aligned}$$

The introduced system model serves as a mathematical fundament for the analysis in this work.

Chapter 3

Reuse-Partitioning Optimization

3.1 Optimization Problem

Typically, ICI mitigation techniques are confronted with the problem that enhanced cell-edge performance is traded off against overall system throughput [1, 5, 6, 14, 24, 25]. Thus, optimization of such schemes aims at maximizing overall throughput while maintaining a minimum performance at cell-edge and minimizing peak-performance loss, represented here by the peak-to-edge ratio. Overall throughput, however, doesn't provide information about the single users' performance and therefore, optimization in this work aims at maximizing the average per-user throughput. For the analysis, per-user throughput is replaced by the concept of capacity density, as seen in Section 3.2.

3.1.1 General Problem Formulation

Such a constrained optimization problem can be described as:

$$\begin{aligned} \max \quad & \bar{c} \\ \text{subject to} \quad & c_{5\%} \geq c_1 \\ & \frac{c_{95\%}}{c_{5\%}} \geq c_2, \end{aligned} \tag{3.1}$$

where \bar{c} denotes the average capacity density (defined in Section 3.2.5). It acts as performance metric for the optimization target and gives a theoretical upper bound for the average per-user throughput. The constants c_1 and c_2 constrain the cell-edge capacity and the peak-to-edge capacity ratio. They set lower limits on the performance at cell-edge and the peak-performance loss, represented here by the peak-to-edge ratio. This general formulation of the capacity optimization problem, suitable for all kinds of ICI mitigation techniques, is in this work utilized in the context of FFR.

3.1.2 Reuse-Partitioning Optimization Problem

An FFR partitioning-scheme splits the cell and the total available bandwidth B_{TOT} in two parts: center and edge. While the center, called FR zone employs $\text{FRF} = 1$, the edge, called PR zone, utilizes a higher order FRF. According to the common assumption in literature [6–9, 13, 14, 16, 17], $\text{FRF} = 3$ is used in this work. As shown in Figure 3.1, FFR completely isolates the cell-edge- and center frequency-bands. Therefore, it holds

$$B_{\text{TOT}} = B_{\text{FR}} + 3B_{\text{PR}}, \quad (3.2)$$

and the PR-bandwidth can be written as a function of B_{FR} and B_{TOT} :

$$B_{\text{PR}}(B_{\text{FR}}, B_{\text{TOT}}) = \frac{B_{\text{TOT}} - B_{\text{FR}}}{3}. \quad (3.3)$$

The normalized FR- and PR-bandwidth are defined as

$$\beta_{\text{FR}} = \frac{B_{\text{FR}}}{B_{\text{TOT}}} \quad (3.4)$$

$$\beta_{\text{PR}}(\beta_{\text{FR}}) = \frac{1 - \beta_{\text{FR}}}{3}, \quad (3.5)$$

where $\beta_{\text{FR}} \in [0, 1]$.

The partitioning boundary ρ separates the FR zone and the PR zone.

The FFR partitioning scheme is then parametrized by the pair $(\rho, \beta_{\text{FR}})$. Now,

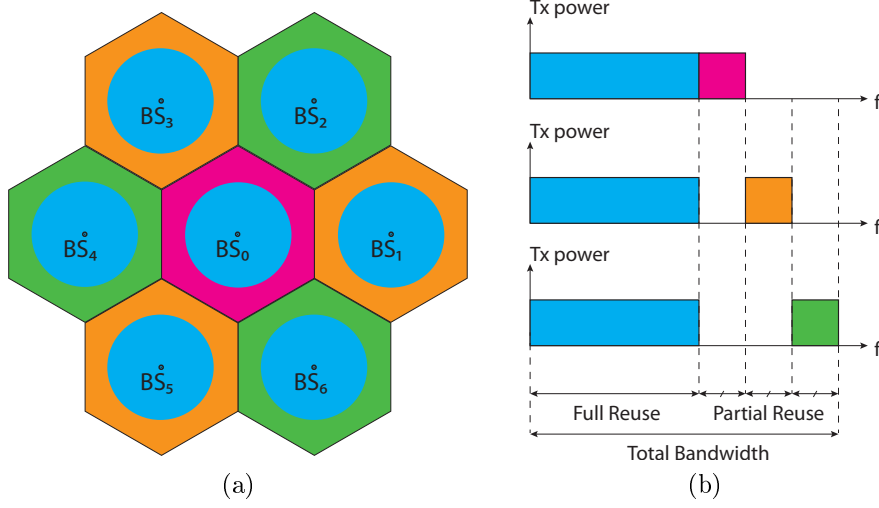


Figure 3.1: An FFR scheme using reuse-3: (a) Cell cluster (b) Bandwidth partitioning

the aim of FFR is to find the optimal pair $(\rho^*, \beta_{\text{FR}}^*)$ ¹ to maximize the constrained average per-user throughput (Equation (3.1)).

Thus, in the context of FFR, the optimization problem of Equation (3.1) can be discretized to

$$\begin{aligned}
 & \max \quad \bar{c}(\rho, \beta_{\text{FR}}) \\
 & \text{subject to} \quad 0 \leq \beta_{\text{FR}} \leq 1 \\
 & \quad \rho \in \mathcal{A}_{\text{cell}} \\
 & \quad c_{5\%} \geq c_1 \\
 & \quad \frac{c_{95\%}}{c_{5\%}} \geq c_2,
 \end{aligned} \tag{3.6}$$

where the first two constraints represent the FFR scheme and the rest the cell-edge and peak-to-edge constraints. $\mathcal{A}_{\text{cell}}$ denotes the cell region. The average capacity density $\bar{c}(\rho, \beta_{\text{FR}})$ as a measure for the average per-user throughput is defined in Section 3.2.5.

¹The symbol * indicates optimal values in terms of the optimization problem

3.2 Assumptions and Simplifications

3.2.1 Noise and Interference Limitation

An FFR partitioning scheme exclusively allocates one part of the available bandwidth B_{TOT} to FR and the remaining part to PR (Figure 3.1). Thus, considering a single cell, no interference exists between center and edge.

In the FR zone, throughput performance is limited by interference of the adjacent BSs (i.e. interference limitation). For the PR zone, it is commonly assumed in literature ([1, 16]) that, due to the higher order reuse, interference is not present (i.e. noise limitation). The SINR at position (x, y) for a given partitioning boundary ρ is thus expressed in terms of the following piecewise function:

$$\gamma_{\rho}(x, y) = \begin{cases} \frac{\Gamma_e}{(x^2+y^2)^{\alpha/2}[1+\Gamma_e S(x,y)]}, & (x, y) \in \text{FR zone} \\ \frac{\Gamma_e}{(x^2+y^2)^{\alpha/2}}, & (x, y) \in \text{PR zone} \end{cases}, \quad (3.7)$$

where Γ_e is the SNR at cell border and $S(x, y)$ is a distance measure as defined in Equations (2.5) and (2.6).

3.2.2 Circular Symmetry

It is still left how to express the partitioning boundary ρ , which separates the center- and edge zones.

Assuming a full-reuse only setup, an exemplary SINR map with constant-SINR contours is given in Figure 3.2. Near the BS, the contours are approximately circular and tend to a quasi-hexagonal form for low SINR values. For further analysis, this motivates the usage of a circular partitioning boundary and therefore, ρ will refer to the boundary radius.

By considering a circular cell boundary of radius R and by taking $x = r$, $y = 0$ (polar coordinates at 0°), the SINR expression in Equation (3.7) is simplified to

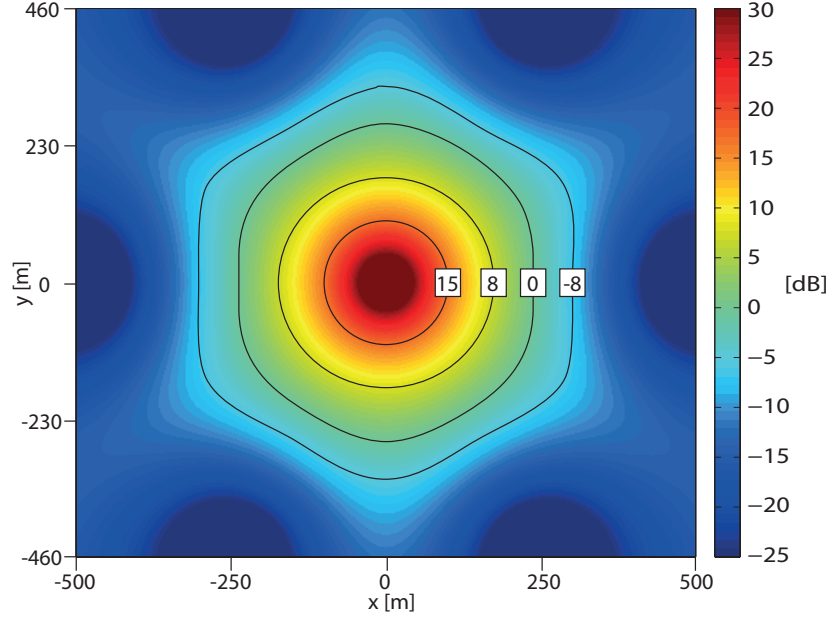


Figure 3.2: Exemplary full-reuse SINR-map with constant-SINR contours

$$\gamma_\rho(r) = \begin{cases} \frac{\Gamma_e}{r^\alpha [1 + \Gamma_e s(r)]}, & 0 < r \leq \rho \\ \frac{\Gamma_e}{r^\alpha}, & \rho < r \leq 1, \end{cases} \quad (3.8)$$

where r and ρ are normalized to R and $s(r)$ is obtained from Equation (2.6) by $s(r) = S(r, 0)$, which then reads

$$\begin{aligned} s(r) = & \left(r - \sqrt{3}\right)^{-\alpha} + \left(r + \sqrt{3}\right)^{-\alpha} \\ & + 2 \left[\left(r - \frac{\sqrt{3}}{2}\right)^2 + \frac{9}{4} \right]^{-\alpha/2} + 2 \left[\left(r + \frac{\sqrt{3}}{2}\right)^2 + \frac{9}{4} \right]^{-\alpha/2}. \end{aligned} \quad (3.9)$$

3.2.3 Bandwidth Density and Capacity Density

Now, consider the following observation: With the assumption of circular symmetry, the area of the FR zone is calculated as $A_{\text{FR}}(\rho) = \rho^2 \pi$. Users within this zone share the bandwidth B_{FR} . By increasing ρ and thus, the coverage of the FR zone, a higher number of users is assigned to this band-

width.

To take this into account in the analysis, a normalized² *bandwidth density* $b_{\rho, \beta_{\text{FR}}}(r)$ (Hz/Unit of Surface) is defined as

$$b_{\rho, \beta_{\text{FR}}}(r) = \begin{cases} \frac{\beta_{\text{FR}}}{A_{\text{FR}}(\rho)}, & 0 < r \leq \rho \\ \frac{\beta_{\text{PR}}(\beta_{\text{FR}})}{A_{\text{PR}}(\rho)}, & \rho < r \leq 1, \end{cases}$$

where $A_{\text{PR}}(\rho) = (1 - \rho^2)\pi$, β_{FR} and $\beta_{\text{PR}}(\beta_{\text{FR}})$ are referred from Equations (3.4) and (3.5) and r and ρ are normalized to the cell radius R . Then, a user at a distance r from the base station achieves a *capacity density* $c_{\rho, \beta_{\text{FR}}}(r)$ (bit/s/Unit of Surface), given by

$$c_{\rho, \beta_{\text{FR}}}(r) = b_{\rho, \beta_{\text{FR}}}(r) \log_2(1 + \gamma_{\rho}(r)), \quad (3.10)$$

where $\gamma_{\rho}(r)$ denotes the SINR. With $b_{\rho, \beta_{\text{FR}}}(r)$ from Equation (3.10) and $\gamma_{\rho}(r)$ from Equation (3.8) it can be rewritten as the following piecewise function:

$$c_{\rho, \beta_{\text{FR}}}(r) = \begin{cases} c_{\text{FR}, \rho, \beta_{\text{FR}}}(r), & 0 < r \leq \rho \\ c_{\text{PR}, \rho, \beta_{\text{PR}}}(r), & \rho < r \leq 1, \end{cases} \quad (3.11)$$

where $c_{\text{FR}, \rho, \beta_{\text{FR}}}(r)$ and $c_{\text{PR}, \rho, \beta_{\text{PR}}}(r)$ are defined as

$$c_{\text{FR}, \rho, \beta_{\text{FR}}}(r) = \frac{\beta_{\text{FR}}}{\rho^2 \pi} \log_2 \left(1 + \frac{\Gamma_e}{r^\alpha [1 + \Gamma_e s(r)]} \right), \quad (3.12)$$

$$c_{\text{PR}, \rho, \beta_{\text{PR}}}(r) = \frac{\beta_{\text{PR}}(\beta_{\text{FR}})}{(1 - \rho^2) \pi} \log_2 \left(1 + \frac{\Gamma_e}{r^\alpha} \right). \quad (3.13)$$

Note, that for FR interference limitation is assumed, while for PR noise limitation is assumed.

²Throughout this work, normalized bandwidth $\beta_{\text{FR}} = B_{\text{FR}}/B_{\text{TOT}}$ is used for the analysis. Therefore, the term *normalized* is obviated for the reader's convenience.

3.2.4 User Density

A user located at (x, y) is either assigned to the FR- or PR zone. The zones differ in allocated bandwidth (see Equations (3.4) and (3.5)) and experienced SINR (see Equations (3.7) and (3.8)). Thus, the position of the users influences the optimal bandwidth allocation and whether a user should be allocated to the FR- or PR zone.

Let us describe the user distribution by a user-density function $u(x, y)$ (Users/Unit of Surface). Then, the number of users in a cell is calculated as

$$N_{\text{users}} = \iint_{\mathcal{A}_{\text{cell}}} u(x, y) dx dy, \quad (3.14)$$

where $\mathcal{A}_{\text{cell}} = \{(x, y) \in \text{Cell} - \text{region}\}$. In this work, the user-density is assumed to be constant, i.e. $u(x, y) = u$. Thus, with Equation (3.14), the number of users is obtained as $N_{\text{users}} = u A_{\text{cell}}$, where $A_{\text{cell}} = \iint_{\mathcal{A}_{\text{cell}}} dx dy$ denotes the cell area.

3.2.5 Definition of Average Capacity Density

As a performance metric for the optimization target, the average *capacity density* (bit/s/Unit of Surface) is utilized.

Let us start with the definition of the average *per-user capacity* (bit/s/User):

$$\bar{c}' = \frac{1}{A_{\text{cell}}} \iint_{\mathcal{A}_{\text{cell}}} \frac{c(x, y)}{u(x, y)} dx dy, \quad (3.15)$$

where $c(x, y)$ (bit/s/Unit of Surface) is the capacity density³, as defined in Section 3.2.3 and $u(x, y)$ denotes the user density.

Assuming the user density to be constant ($u(x, y) = u$, i.e. 1 for calculation purposes), Equation (3.15) is expressed as

$$\bar{c} = \frac{1}{A_{\text{cell}}} \iint_{\mathcal{A}_{\text{cell}}} c(x, y) dx dy. \quad (3.16)$$

³Note that (x, y) is used instead of the radius $r = \sqrt{x^2 + y^2}$

Then, for the analysis of the optimization problem, the concept of *per-user capacity* and *capacity density* (i.e. per-area capacity) are fully equivalent. In this work, the user density is therefore obviated and capacity density \bar{c} (bit/s/m²) is employed as performance metric. Further, cell-edge capacity $c_{5\%}$ and peak capacity $c_{95\%}$ also refer to per-area capacity densities (bit/s/m²).

3.2.6 Average Reuse-Partitioning Capacity Density

Let us formulate the average capacity density in terms of FFR. Obviating the user density in Equation (3.15), it is calculated as

$$\bar{c}(\rho, \beta_{\text{FR}}) = \frac{1}{A_{\text{cell}}} \left[\iint_{\mathcal{A}_{\text{FR}}(\rho)} c_{\text{FR},\rho,\beta_{\text{FR}}}(x, y) dx dy + \iint_{\mathcal{A}_{\text{PR}}(\rho)} c_{\text{PR},\rho,\beta_{\text{PR}}}(x, y) dx dy \right], \quad (3.17)$$

where $\mathcal{A}_{\text{FR}}(\rho)$ and $\mathcal{A}_{\text{PR}}(\rho)$ are the regions of the FR- and PR zone. With the corresponding areas $A_{\text{FR}}(\rho)$ and $A_{\text{PR}}(\rho)$, the cell area is obtained as $A_{\text{cell}} = A_{\text{FR}}(\rho) + A_{\text{PR}}(\rho)$. The terms $c_{\text{FR},\rho,\beta_{\text{FR}}}(x, y)$ and $c_{\text{PR},\rho,\beta_{\text{PR}}}(x, y)$ denote the capacity densities in the FR- and PR zone:

$$c_{\text{FR},\rho,\beta_{\text{FR}}}(x, y) = \frac{B_{\text{FR}}}{A_{\text{FR}}(\rho)} \log_2 (1 + \text{SINR}_{\text{FR}}(x, y)) \quad (3.18)$$

$$c_{\text{PR},\rho,\beta_{\text{PR}}}(x, y) = \frac{B_{\text{PR}}}{A_{\text{PR}}(\rho)} \log_2 (1 + \text{SINR}_{\text{PR}}(x, y)). \quad (3.19)$$

With the assumption of circular symmetry, Equation (3.17) can equivalently be expressed as

$$\bar{c}(\rho, \beta_{\text{FR}}) = \frac{B_{\text{TOT}}}{\pi} \left[\int_0^\rho c_{\text{FR},\rho,\beta_{\text{FR}}}(r) 2\pi r dr + \int_\rho^1 c_{\text{PR},\rho,\beta_{\text{PR}}}(r) 2\pi r dr \right], \quad (3.20)$$

where $c_{\text{FR},\rho,\beta_{\text{FR}}}(r)$ and $c_{\text{PR},\rho,\beta_{\text{PR}}}(r)$ are the capacity densities defined in Equations (3.12) and (3.13) and the partitioning boundary ρ refers to a radius.

Now, the optimization problem states as: "Find the optimal partitioning-boundary radius ρ^* and normalized FR bandwidth β_{FR}^* to maximize the average capacity density with respect to the constraints in Equation (3.6)".

3.3 Optimization Proposal

With the target to maximize the average capacity density, it is proposed in this work, that a given user is allocated either to an FR- or PR zone, according to where the capacity density is higher, which is expressed as:

$$c_{\text{FFR},\rho,\beta_{\text{FR}}}(r) = \max(c_{\text{FR},\rho,\beta_{\text{FR}}}(r), c_{\text{PR},\rho,\beta_{\text{PR}}}(r)). \quad (3.21)$$

This is illustrated in Figure 3.3, where the *capacity densities* for FR (red) and PR (green) are found by applying Equations (3.12) and (3.13) along the center axis of a hexagonal cell. Then, ρ is calculated by solving

$$\begin{aligned} c_{\text{FR},\rho,\beta_{\text{FR}}}(r) &= c_{\text{PR},\rho,\beta_{\text{PR}}}(r) \\ \frac{\beta_{\text{FR}}}{\rho^2\pi} \log_2 \left(1 + \frac{\Gamma_e}{r^\alpha [1 + \Gamma_e s(r)]} \right) &= \frac{\frac{1}{3}(1 - \beta_{\text{FR}})}{(1 - \rho^2)\pi} \log_2 \left(1 + \frac{\Gamma_e}{r^\alpha} \right) \end{aligned} \quad (3.22)$$

to the variable r . It is unique for any given combination of B_{FR} , B_{PR} and B_{TOT} . Since B_{TOT} is constant and B_{FR} and B_{PR} are coupled by Equation (3.2), a mapping between ρ and β_{FR} can be obtained from Equation (3.22).

Figure 3.4 shows the resulting mapping, obtained by exhaustive search of

$$\rho(\beta_{\text{FR}}) = \arg \min_{\rho} |c_{\text{FR},\rho,\beta_{\text{FR}}}(r) - c_{\text{PR},\rho,\beta_{\text{PR}}}(r)|. \quad (3.23)$$

The difference $|c_{\text{FR},\rho,\beta_{\text{FR}}}(r) - c_{\text{PR},\rho,\beta_{\text{PR}}}(r)|$ is depicted in a logarithmic scale. There, the minimum can be seen as a deep blue line and the mapping thus obtained is figured out to be an injective function. Thus, the mapping

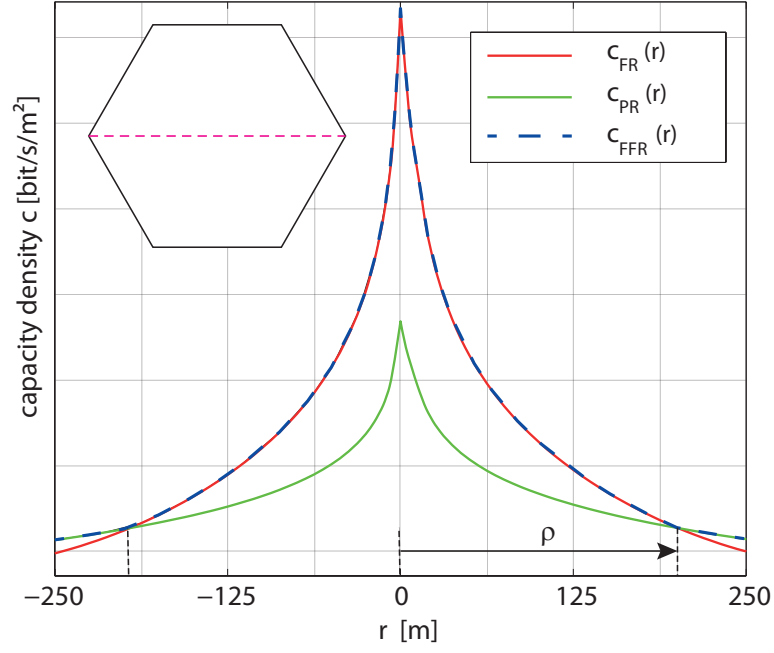


Figure 3.3: Capacity densities and switching radius ρ , $R = 250$ m

can be implemented as a look-up table, used as shown in Figures 4.2 and 4.8.

Now, instead of optimizing a value pair $(\rho, \beta_{\text{FR}})$, the FFR partitioning scheme is parametrized by either ρ or β_{FR} , i.e. the average capacity density $\bar{c}(\rho, \beta_{\text{FR}})$ can equivalently be expressed as $\bar{c}(\beta_{\text{FR}})$ or $\bar{c}(\rho)$.

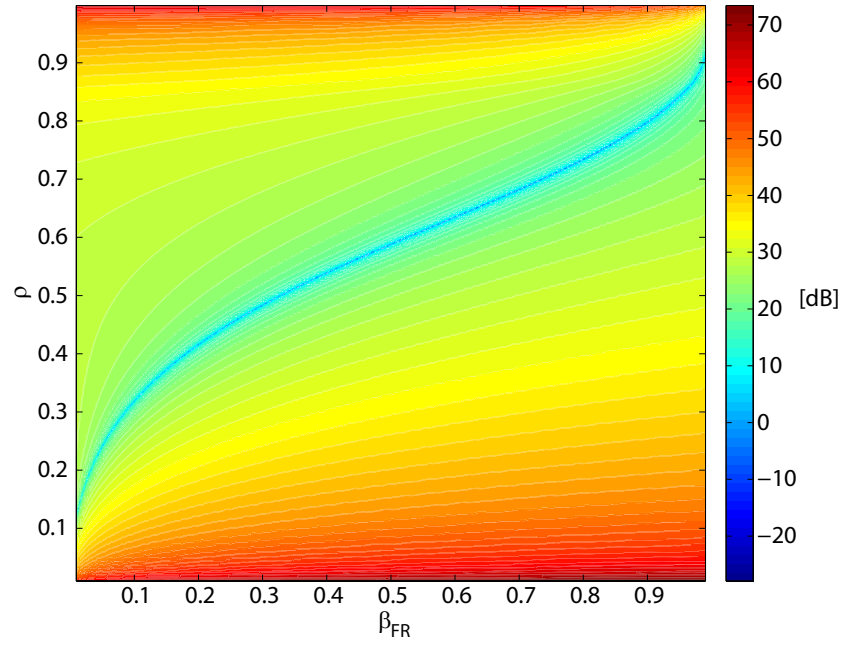


Figure 3.4: Exhaustive search for mapping $\rho(\beta_{\text{FR}})$: $|c_{\text{FR},\rho,\beta_{\text{FR}}}(r) - c_{\text{PR},\rho,\beta_{\text{PR}}}(r)|$

Chapter 4

Simulation Results of Omnidirectional Scenarios

The FFR-optimization problem of Equation (3.6) (Section 3.1) is now investigated by simulations. With the obtained mapping function $\rho(\beta_{\text{FR}})$ of Section 3.3, it is formulated as

$$\begin{aligned} \max \quad & \bar{c}(\beta_{\text{FR}}) \\ \text{subject to} \quad & 0 \leq \beta_{\text{FR}} \leq 1 \\ & 0 \leq \rho \leq 1 \\ & c_{5\%} \geq c_1 \\ & \frac{c_{95\%}}{c_{5\%}} \geq c_2, \end{aligned} \tag{4.1}$$

where the average capacity density $\bar{c}(\rho, \beta_{\text{FR}})$ becomes $\bar{c}(\beta_{\text{FR}})$.

4.1 Simulation Setup

In this setting, a cluster of equidistantly spread, omnidirectional-radiating BSs is used (see Figure 4.1). For this, the following assumptions have been done:

Cell radius R	250	m
Total bandwidth B_{TOT}	5	MHz
Center frequency f_c	2	GHz
Noise spectral density N_0	-174	dBm
Path loss exponent α	3.6	-
Total power P_{TOT}	20	W

Table 4.1: Simulation parameters of omnidirectional scenarios (Cell radius R referred from [4])

- A grid of hexagonal cells with radius R
- Each BS is equipped with an omnidirectional antenna with 0 dB gain
- A worst-case interference situation, where all interfering BSs are transmitting at the maximum available power
- Constant user density within the cells

The results are evaluated for the center cell (BS_0), while the surrounding cells serve as interferers. The simulation parameters are listed in Table 4.1.

Simulations are carried out for two scenarios: A one-ring scenario, where the center cell is surrounded by one tier of direct neighbor BSs and a two-rings scenario, which considers an inner and an outer ring of neighboring BSs.

Both scenarios employ $\text{FRF} = 1$ in the FR zone. However, in the one-ring scenario, the PR zone is noise limited, as commonly stated in literature [1, 16], whereas in the two-rings scenario, the effect of the interference is also extended to the PR zone. In both cases, $\text{FRF} = 3$ is employed in the PR zone.

The FFR partitioning-scheme is compared to a conventional reuse-1- ($\text{FRF} = 1$) and reuse-3 scheme ($\text{FRF} = 3$) [26, 27]. Both conventional schemes apply the simulation parameters given in Table 4.1 and a cell grid according to the scenario, i.e. one or two tiers of surrounding BSs.

4.2 Calculation Methods

The average capacity densities of the three schemes are calculated in MATLAB as

$$\bar{c}_{\text{Reuse-1}} = \frac{1}{\#_{\text{cell}}} \sum_{\mathcal{A}_{\text{cell}}} \frac{B_{\text{TOT}}}{\#_{\text{cell}} a_{\text{pp}}} \log_2 (1 + \text{SINR}_{\text{FRF1}}) \quad (4.2)$$

$$\bar{c}_{\text{Reuse-3}} = \frac{1}{\#_{\text{cell}}} \sum_{\mathcal{A}_{\text{cell}}} \frac{1}{3} \frac{B_{\text{TOT}}}{\#_{\text{cell}} a_{\text{pp}}} \log_2 (1 + \text{SINR}_{\text{FRF3}}) \quad (4.3)$$

$$\begin{aligned} \bar{c}_{\text{FFR}}(\rho, \beta_{\text{FR}}) = \frac{1}{\#_{\text{cell}}} & \left[\sum_{\mathcal{A}_{\text{FR}}(\rho)} \frac{\beta_{\text{FR}} B_{\text{TOT}}}{\#_{\text{FR}}(\rho) a_{\text{pp}}} \log_2 (1 + \text{SINR}_{\text{FRF1}}) \right. \\ & \left. + \sum_{\mathcal{A}_{\text{PR}}(\rho)} \frac{1 - \beta_{\text{FR}}}{3} \frac{B_{\text{TOT}}}{\#_{\text{PR}}(\rho) a_{\text{pp}}} \log_2 (1 + \text{SINR}_{\text{FRF3}}) \right], \end{aligned} \quad (4.4)$$

where a_{pp} is the pixel size (m^2/pixel), $\#$ denotes the number of pixels in a given region and \mathcal{A} the pixels within.

Edge capacity ($c_{5\%}$) and peak capacity ($c_{95\%}$) are used as measures for cell-edge- and peak performance. The values are found by calculating the capacity-density ECDF of the center cell (see Figure 1.3 in Chapter 1).

4.3 One-Ring Scenario

A cluster composed of a center cell BS_0 and six direct neighbors $\text{BS}_1 \dots \text{BS}_6$ is assumed. Such a cluster is depicted in Figure 4.1. In this simulation setup, the PR zone of the center cell doesn't experience CCI due to employing $\text{FRF} = 3$. It is therefore noise limited. This also holds for the conventional reuse-3 scheme, which is used for comparison.

Let us start with the mapping $\rho(\beta_{\text{FR}})$. According to Section 3.3, it is obtained by exhaustive search for $c_{\text{FR},\rho,\beta_{\text{FR}}}(r) = c_{\text{PR},\rho,\beta_{\text{FR}}}(r)$ (Equation (3.22)) over ρ and β_{FR} . Figure 4.2 depicts the numerical result of $\rho(\beta_{\text{FR}}) = \arg \min_{\rho} |c_{\text{FR},\rho,\beta_{\text{FR}}}(r) - c_{\text{PR},\rho,\beta_{\text{PR}}}(r)|$ (Equation (3.23)).

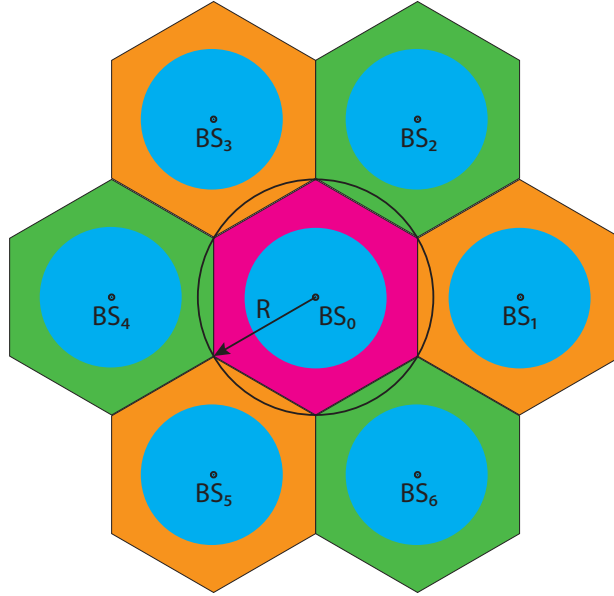


Figure 4.1: One-ring scenario with sector assignment. FR zone depicted in blue. PR zones depicting the employed reuse-3 scheme

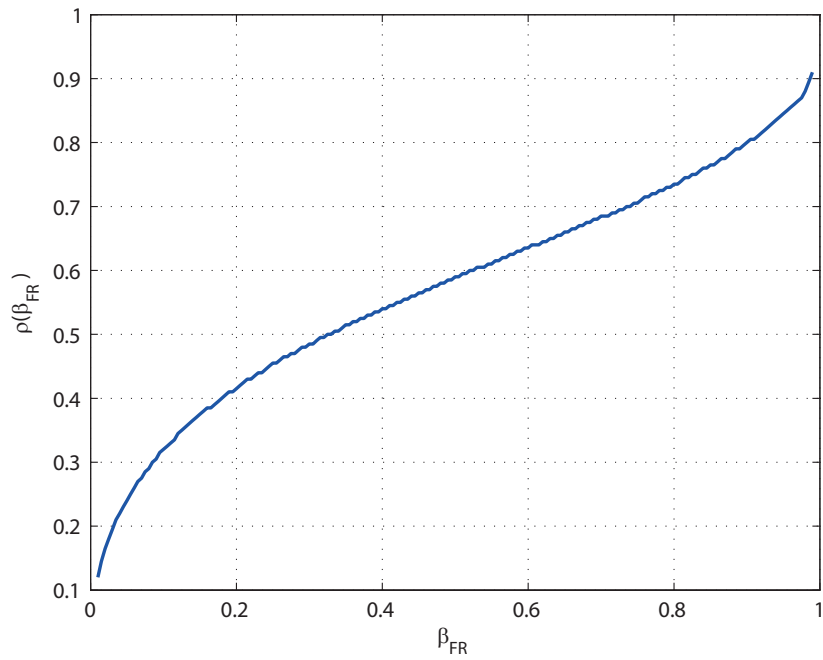


Figure 4.2: Mapping $\rho(\beta_{FR})$ in one-ring scenario

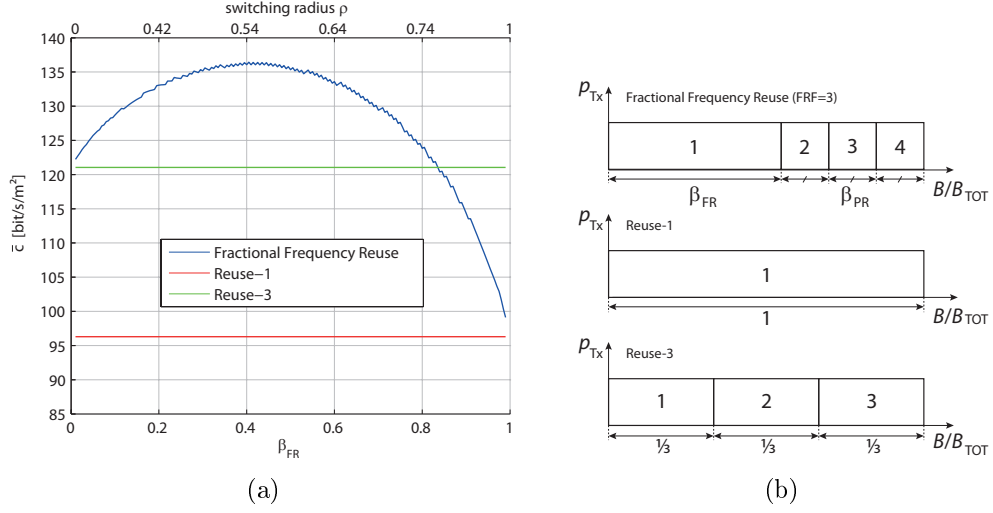


Figure 4.3: (a) Average capacity densities in one-ring scenario. FFR depicted in blue. Red and green lines depict reuse-1- and reuse-3 average per-user capacities respectively. (b) Bandwidth allocation of FFR, reuse-1 and reuse-3

With the obtained mapping, the FFR scheme is parametrized by β_{FR} only. Thus, the average capacity density $\bar{c}_{FFR}(\rho, \beta_{FR})$ in Equation (4.4) can be expressed as $\bar{c}_{FFR}(\beta_{FR})$.

Figure 4.3a depicts the average capacity density $\bar{c}_{FFR}(\beta_{FR})$ compared with the average capacity densities when using a reuse-1 (Equation (4.2)) and reuse-3 (Equation (4.3)) scheme. While reuse-1 is expected to give the best performance in terms of overall capacity ([7]), results show that it is outperformed by both FFR and reuse-3.

This result is, however, caused by the fact that noise limitation is assumed in the PR zone, as commonly found in literature ([1, 16]). This assumption critically influences the result and motivates investigations on the influence of the interference- and noise powers.

4.4 Noise Power versus Interference Power

In the one-ring scenario, the center cell doesn't experience CCI for FRF = 3. In order to add CCI to the PR zone, the one-ring cell cluster (see Figure 4.1)

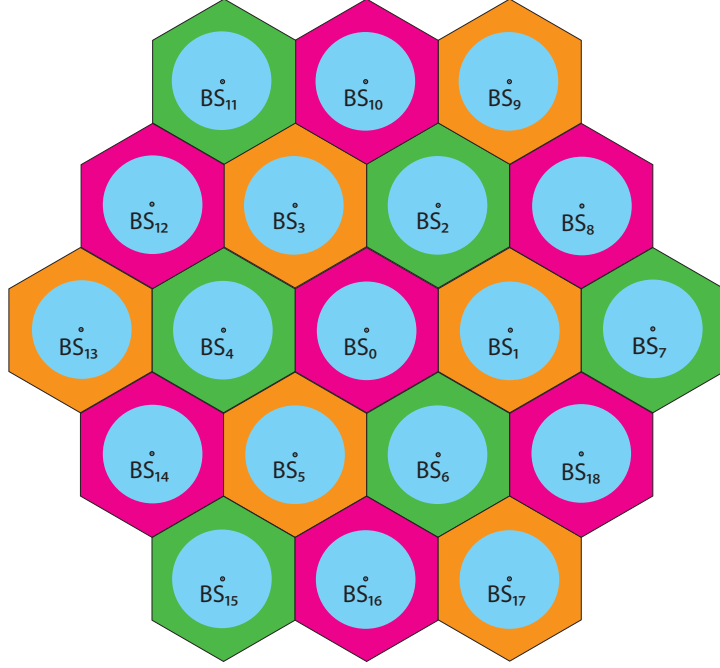


Figure 4.4: Two-rings scenario with sector assignment. FR zone depicted in blue. PR zones depicting the employed $\text{FRF} = 3$.

is extended by an outer ring of BSs ($\text{BS}_7 \dots \text{BS}_{18}$), as shown in Figure 4.4.

Here, also a worst case CCI scenario is assumed, i.e. each BS transmits with a constant power density p_{Tx} (W/Hz) (see Chapter 2).

Let us denote the received power density of the useful signal from BS_0 as $p_{\text{Rx},0}(x, y)$. Then, the interferer power densities for $\text{FRF} = 1$ and $\text{FRF} = 3$ at position (x, y) are expressed as

$$p_{\text{CCI,FRF1}}(x, y) = \sum_{i=1}^{18} p_{\text{Rx},i}(x, y) \quad (4.5)$$

$$p_{\text{CCI,FRF3}}(x, y) = \sum_{i \in \mathcal{I}} p_{\text{Rx},i}(x, y), \quad (4.6)$$

where $p_{\text{Rx},i}(x, y)$ is the received power density from BS_i . The numbers i refer to the sector assignment, as shown in Figure 4.4, where $\mathcal{I} = \{8, 10, 12, 14, 16, 18\}$ denotes the interfering BSs for $\text{FRF} = 3$.

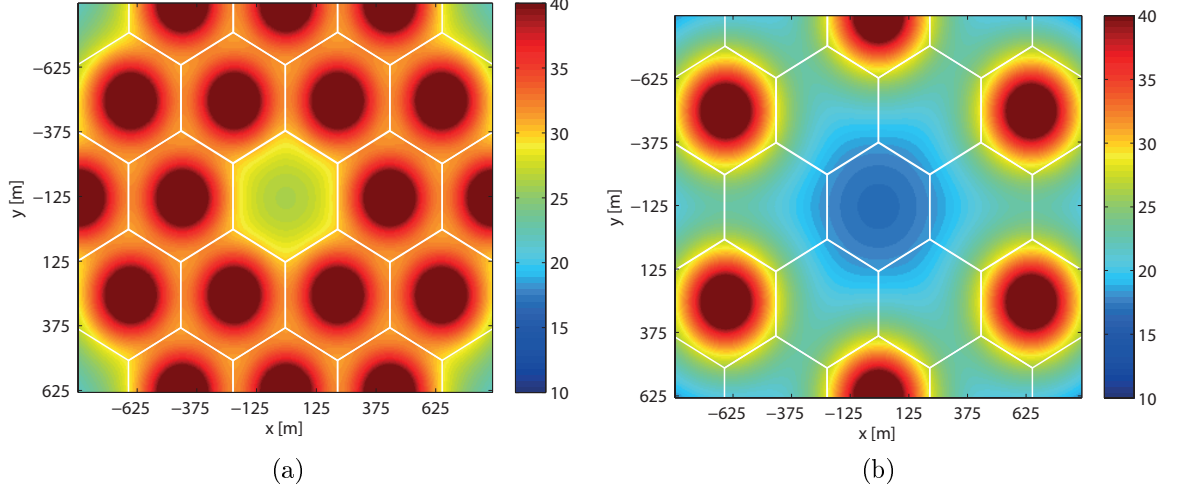


Figure 4.5: Comparison of signal- and noise power density (a) reuse-1: $p_{\text{CCI,FRF1}}(x,y)/N_0$ (dB), (b) reuse-3: $p_{\text{CCI,FRF3}}(x,y)/N_0$ (dB)

The interferer power densities can now be compared to the noise spectral density N_0 . Figures 4.5a and 4.5b show the spectral density of the received interfering power relative to the one from noise. It is depicted for both the FR zone ($p_{\text{CCI,FRF1}}(x,y)/N_0$ (dB)) in (a) and the PR zone ($p_{\text{CCI,FRF3}}(x,y)/N_0$ (dB)) in (b). Figure 4.6 shows a horizontal cut from Figure 4.5b along the center axis of the cell cluster.

It can be seen that the minimum interferer power density lies approximately 17 dB above the noise spectral density. Thus, in contrast to the common assumptions, reuse-3 is interference limited for the given system setup.

Let us increase the distance between the BSs by setting the cell radius to $R = 500$ m. Like before, $p_{\text{CCI,FRF3}}(x,y)/N_0$ (dB) is applied along the cluster's horizontal center axis, shown in Figure 4.7. Now, the interferer power density lies at least 6 dB above the noise level. Thus, interference limitation even holds when doubling the distance between BSs.

This motivates to redo simulations, as presented in Section 4.3, in a two-rings scenario.

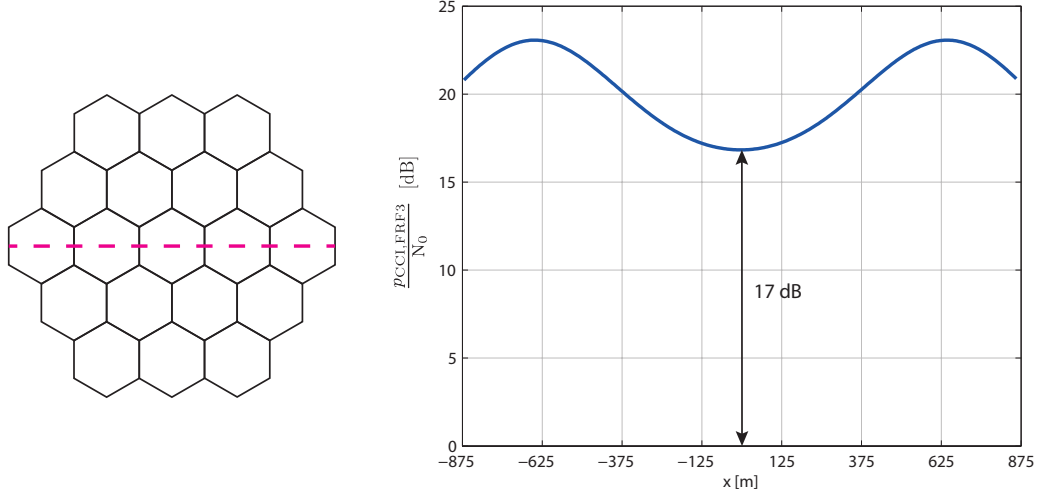


Figure 4.6: $p_{\text{CCI,FRF3}}(x, y)/N_0$ (dB) along the horizontal center axis of the cell cluster; $R = 250$ m

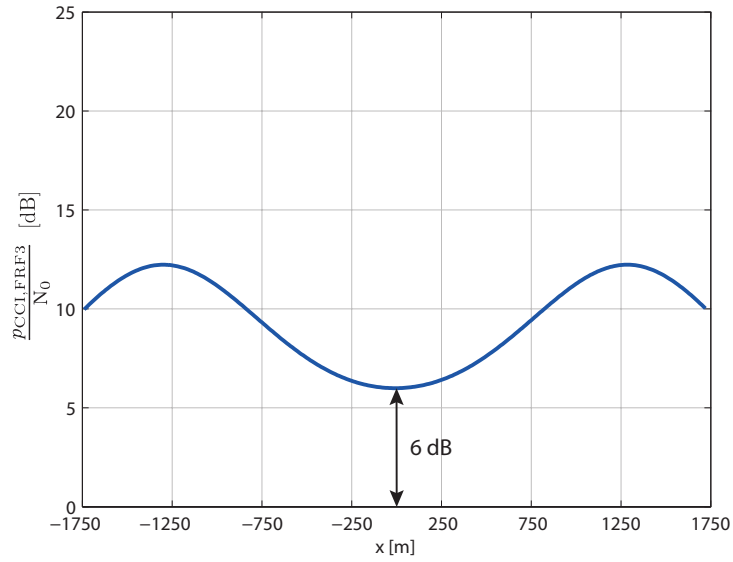


Figure 4.7: $p_{\text{CCI,FRF3}}(x, y)/N_0$ (dB) along the horizontal center axis of the cell cluster; $R = 500$ m

4.5 Two-Rings Scenario

The cell cluster of a two-rings scenario is composed of a center cell (BS_0), an inner ring of six direct neighbors $BS_1 \dots BS_6$, and an outer ring $BS_7 \dots BS_{18}$, as shown in Figure 4.4. With the parameters of Table 4.1, simulations are carried out for the reuse-3 FFR scheme.

In contrast to the one-ring scenario, the center cell now experiences CCI also for $FRF = 3$. It is therefore interference limited.

First of all, the mapping $\rho(\beta_{FR})$ is recalculated as in Section 3.3. In terms of a two-rings scenario, the FR- and PR capacity densities, as defined in Equations (3.12) and (3.13), are reformulated as

$$c_{FR,\rho,\beta_{FR}}(r) = \frac{\beta_{FR}}{\rho^2\pi} \log_2 \left(1 + \frac{p_{Rx,0}(r)}{N_0 + p_{CCI,FRF1}(r)} \right) \quad (4.7)$$

$$c_{PR,\rho,\beta_{PR}}(r) = \frac{\frac{1}{3}(1 - \beta_{FR})}{(1 - \rho^2)\pi} \log_2 \left(1 + \frac{p_{Rx,0}(r)}{N_0 + p_{CCI,FRF3}(r)} \right), \quad (4.8)$$

where $p_{CCI,FRF1}(r) = p_{CCI,FRF1}(r, 0)$ and $p_{CCI,FRF3}(r) = p_{CCI,FRF3}(r, 0)$ are obtained from Equations (4.5) and (4.6) by assuming circular symmetry. The mapping $\rho(\beta_{FR})$, depicted in Figure 4.8, is obtained by solving Equation (3.23).

Figure 4.9a shows the calculated average capacity densities (left y-axis) and their gain relative to reuse-1 (right y-axis)¹. As expected, reuse-1 now outperforms reuse-3. For $\beta_{FR} > 0.52$, simulation results show that the FFR scheme outperforms reuse-1 and reuse-3 in terms of average capacity density.

In the next step, the optimization constraints $c_{5\%} \geq c_1$ and $c_{95\%}/c_{5\%} \geq c_2$ (Equation (4.1)) are investigated. Thereto, Figures 4.9b, 4.10a, and 4.10b show the simulation results for cell-edge capacity ($c_{5\%}$), peak capacity ($c_{95\%}$) and peak-to-edge capacity ratio ($c_{95\%}/c_{5\%}$). With the additional y-axis on the right hand side of the figures, the corresponding relative gain in comparison to reuse-1 can be figured out.

In terms of cell-edge capacity density, reuse-1 is outperformed by reuse-3.

¹Relative values are calculated as $(x - x_{ref})/x_{ref}$, where x_{ref} is the reference value.

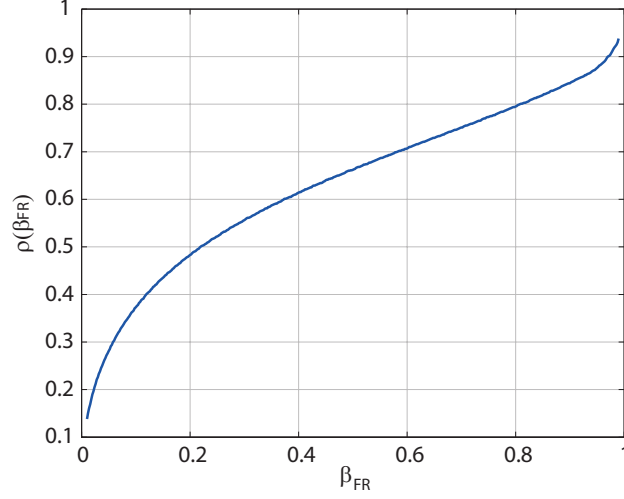


Figure 4.8: Mapping $\rho(\beta_{\text{FR}})$ in two-rings scenario

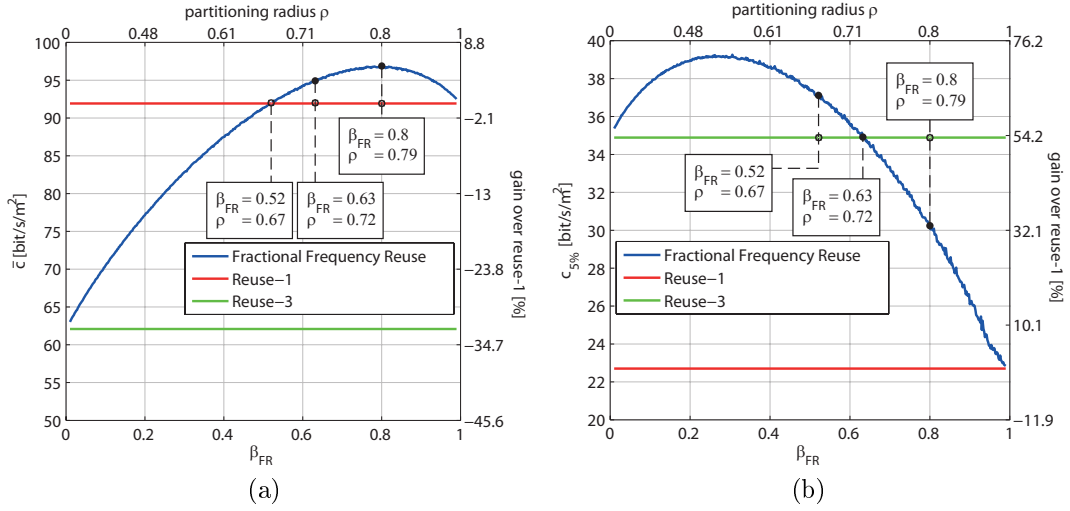


Figure 4.9: (a) Average capacity densities (\bar{c}) and (b) cell-edge capacities ($c_{5\%}$) in two-rings scenario. FFR depicted in blue. Red and green lines depict capacity densities of reuse-1 and reuse-3. Labels denoting points, where FFR achieves no average performance loss compared to reuse-1 ($\beta_{\text{FR}} = 0.52$), reuse-3 equivalent cell-edge performance ($\beta_{\text{FR}} = 0.63$) and maximum average capacity density ($\beta_{\text{FR}} = 0.8$).

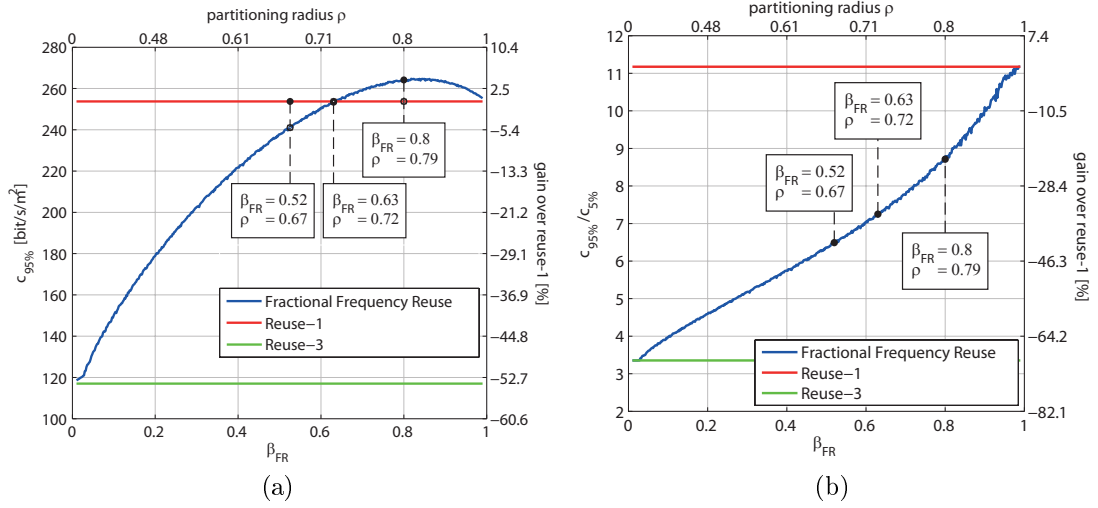


Figure 4.10: (a) Peak capacities ($c_{95\%}$) and (b) peak-to-edge ratio ($c_{95\%}/c_{5\%}$) in two-rings scenario. FFR depicted in blue. Red and green lines depict capacity densities (a) and ratios (b) of reuse-1 and reuse-3.

Nevertheless, for $\beta_{FR} < 0.63$, FFR exceeds both conventional schemes in terms of cell-edge capacity.

Let us go into further detail by calculating the capacity density ECDFs at an exemplary point $\beta_{FR} = 0.8$, which corresponds to the point where the maximum average capacity density (\bar{c}) is achieved. For this specific bandwidth allocation, in comparison to a reuse-1 scheme, FFR improves \bar{c} by 4.2% while $c_{5\%}$ is 32.7% higher and $c_{95\%}$ is improved by 5.3%, as seen in Figure 4.12. The ECDF curves are shown in Figure 4.11, where the red, green and blue dots denote the average capacity densities for the reuse-1, reuse-3 and FFR case, respectively.

From these curves it is seen that FFR has a slightly lower edge capacity density $c_{5\%}$ than reuse-3, while its peak capacity $c_{95\%}$ is almost equal to reuse-1. Therefore, the peak-to-edge ratio ($c_{95\%}/c_{5\%}$), initially proposed as a constraint and depicted in Figure 4.10b, does not give a meaningful measure for the peak-performance loss and is thus no longer of interest.

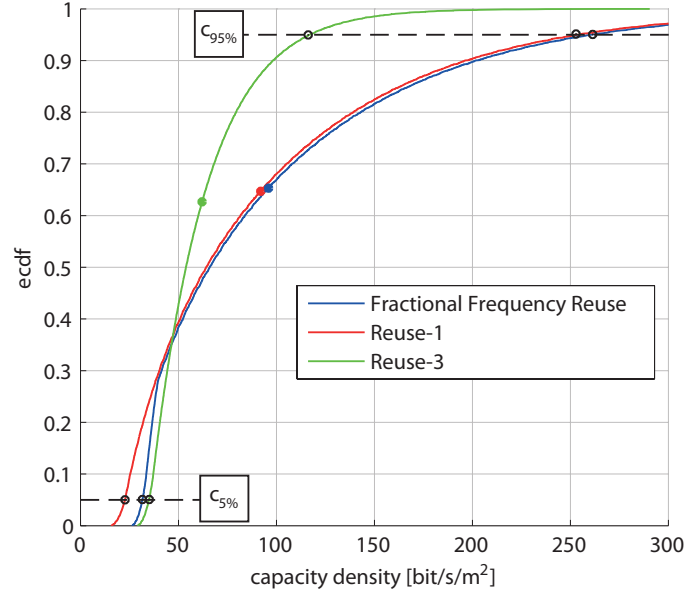


Figure 4.11: ECDF curves of two-rings scenario at $\beta_{\text{FR}} = 0.8$. In comparison to a reuse-1 scheme, FFR improves for this specific bandwidth allocation $c_{5\%}$ by 32.7% while $c_{95\%}$ is 5.3% higher.

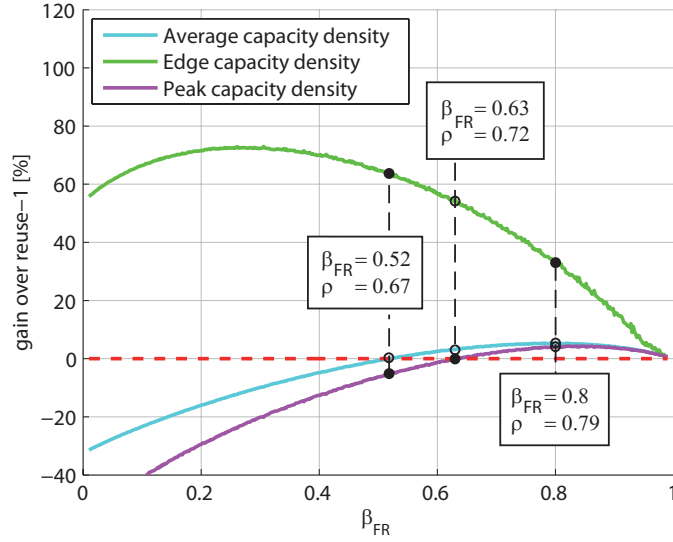


Figure 4.12: Relative capacity density gains of FFR over conventional reuse-1 scheme in two-rings omnidirectional scenario. Labels denoting points, where FFR achieves no average performance loss compared to reuse-1 ($\beta_{\text{FR}} = 0.52$), reuse-3 equivalent cell-edge performance ($\beta_{\text{FR}} = 0.63$) and maximum average capacity density ($\beta_{\text{FR}} = 0.8$).

Chapter 5

Optimization of Reuse Partitioning in Sectorized Scenarios

5.1 Introduction and Cell Design

The FFR partitioning scheme is now applied and optimized in sectorized scenarios. Cell sectoring is a commonly used method of increasing cellular capacity in mobile networks. In a sectorized scenario, each site is equipped with three BSs (it could be more, albeit this is the most commonly used number [2, 6, 16, 28, 29]), each equipped with directional antennas. A cell is then composed of three hexagonally shaped sectors, as shown in Figure 5.1a.

As in omnidirectional scenarios, the optimization problem formulates:

$$\begin{aligned} \max \quad & \bar{c}(\rho, \beta_{\text{FR}}) \\ \text{subject to} \quad & 0 \leq \beta_{\text{FR}} \leq 1 \\ & \rho \in \mathcal{A}_{\text{sector}} \\ & c_{5\%} \geq c_1, \end{aligned} \tag{5.1}$$

where $\bar{c}(\rho, \beta_{\text{FR}})$ is the average capacity density, β_{FR} is the normalized

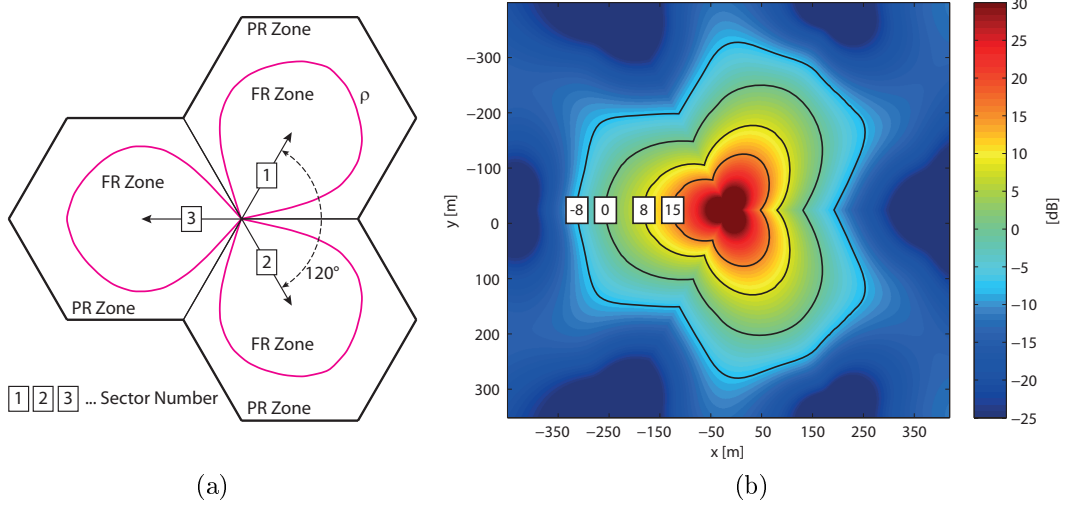


Figure 5.1: (a) Cell design in sectorized scenario (b) SINR map of center site with constant-SINR contours

full-reuse bandwidth (Equation (3.4)) and $c_{5\%}$ denotes the cell-edge capacity.

Each sector, containing a region denoted as $\mathcal{A}_{\text{sector}}$, employs an FR- and PR zone and thus, has its own partitioning boundary ρ . However, the partitioning boundary cannot be simplified to a radius, since the assumption of circular symmetry is not valid anymore. This assumption, applied in the omnidirectional case, is motivated by SINR contours showing up as circles in that situation (see Figure 3.2). As seen from Figure 5.1b, this does not apply to sectorized scenarios.

In the sectorized case, the transmitted power of the useful signal is focused into the corresponding sector. Thereby, also interference in the adjacent cells is reduced. Thus, SINR is determined not only by path loss but also the sector antennas' radiation pattern.

In this chapter, a Two-dimensional (2-D)- and Three-dimensional (3-D) scenario are investigated: In the first, only a horizontal radiation pattern is applied, such as commonly considered in literature [6, 10, 16, 29], whereas the second scenario also considers a vertical radiation pattern, which allows the effect of electrical downtilting to be shown, nowadays almost invariably

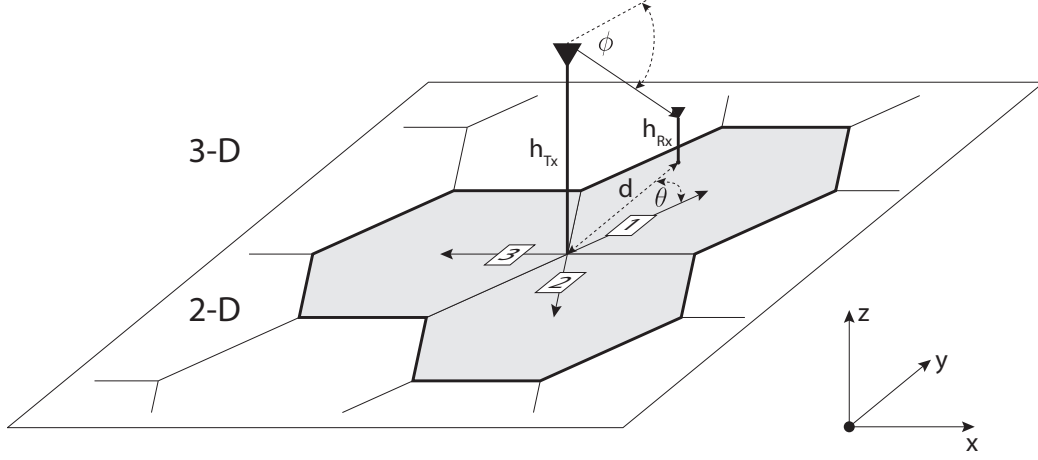


Figure 5.2: 2-D- and 3-D sectorized scenario

used in real system deployments.

5.2 Path Loss and Antenna Radiation Patterns

5.2.1 Propagation Path Loss

The channel power gain between two points separated by a distance d is restricted to the propagation path loss $L(d)|_{\text{dB}}$. Figure 5.5 shows an exemplary path loss map using the exponential path loss model $L(d)|_{\text{dB}} = 20 \log_{10} (c_0 / (4\pi f_c)) - \alpha 10 \log_{10} (d)$, as introduced in Chapter 2.

Now, let $G_{\text{Tx}}(x, y)|_{\text{dB}}$ denote the additional power gain of a directional antenna at position (x, y) . Then, assuming that BS_0 is located at the coordinate origin, the received power density $p_{\text{Rx}}(x, y)$ (dBm/Hz) is expressed as

$$p_{\text{Rx}}(x, y)|_{\frac{\text{dBm}}{\text{Hz}}} = p_{\text{Tx}}|_{\frac{\text{dBm}}{\text{Hz}}} + G_{\text{Tx}}(x, y)|_{\text{dB}} + L\left(\sqrt{x^2 + y^2}\right)|_{\text{dB}}, \quad (5.2)$$

where $p_{\text{Tx}}|_{\frac{\text{dBm}}{\text{Hz}}}$ is the transmit power density.

The antenna gain $G_{\text{Tx}}(x, y)|_{\text{dB}}$ is obtained by the antenna's radiation pattern. It is investigated in the following subsections for the 2-D- and 3-D case.

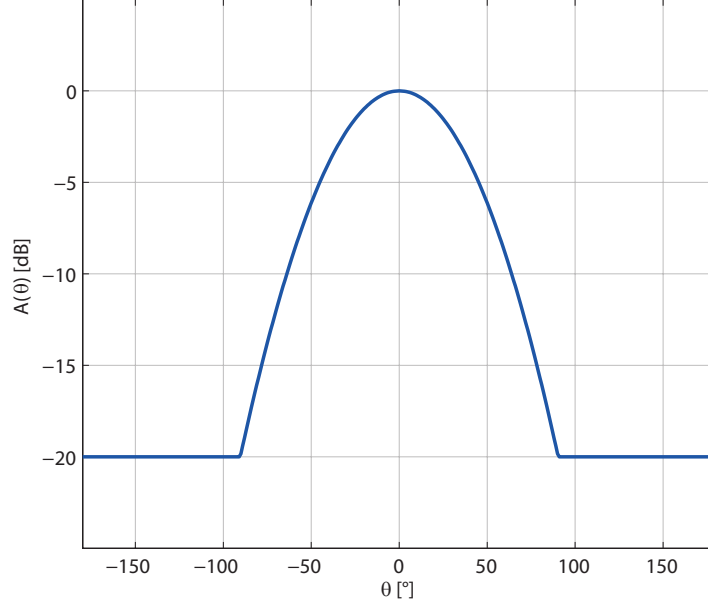


Figure 5.3: Horizontal antenna radiation pattern referred from [2]

5.2.2 Two-dimensional Antenna Radiation Pattern

A 2-D scenario is restricted to a flat plane, i.e. height of transmitter and receiver are neglected, as shown in Figure 5.2. Thus, only the antennas' horizontal radiation pattern is employed.

Two-dimensional antenna radiation patterns, despite of being the most unrealistic choice of the two, are used as a de-facto system environment setting. The pattern applied in this work is referred from [2] and defined as

$$A(\theta) = -\min \left[12 \left(\frac{\theta}{\theta_{3\text{dB}}} \right)^2, A_m \right], \quad -180^\circ \leq \theta < 180^\circ, \quad (5.3)$$

where θ is the horizontal angle, $\theta_{3\text{dB}}$ is the 3 dB beam width, corresponding to 65° and A_m denotes the maximum attenuation. Figure 5.3 shows the radiation pattern with a maximum antenna gain of 0 dB and a maximum attenuation $A_m = 20$ dB.

Then, by determining θ for a given receiver position (x, y) , the antenna gain $G_{\text{Tx}}(x, y)|_{\text{dB}}$ can be calculated.

As an example, Figure 5.6a depicts the antenna gain of the center site's sector

antenna 1. The resulting received power density, shown in Figure 5.7a, is obtained by applying Equation (5.2), where a transmit power density $p_{Tx} = 0$ dBm/Hz is assumed.

5.2.3 Three-dimensional Antenna Radiation Pattern

Let us now extend the 2-D scenario by considering the transmitter's and receiver's height as shown in Figure 5.2. This is referred to as 3-D scenario.

Now, the antenna gain $G_{Tx}(x, y)|_{dB}$ depends on the horizontal angle θ and vertical angle ϕ between transmitter and receiver. Therefore, a horizontal and vertical radiation pattern are employed. An adequate approximation of the antenna gain is then obtained by extrapolating these cuts [30, 31].

In this work, the patterns are taken from a "Kathrein 742 215 Panel Antenna" ([3], Figure 5.4a), as shown in Figure 5.4b in a polar coordinate system. To focus transmit power into the corresponding sector, the antenna is electrically tilted down by 8° . This causes the vertical radiation pattern to skew. Figure 5.6b gives the resulting antenna gain $G_{Tx}(x, y)|_{dB}$, assuming a transmitter height $h_{Tx} = 20$ m and receiver height $h_{Rx} = 1.5$ m.

Then, by setting the transmit power density $p_{Tx} = 0$ dBm/Hz and applying Equation (5.2), the received power density $p_{Rx}(x, y)|_{\frac{dBm}{Hz}}$ is obtained, as shown in Figure 5.7b.

In this way, the received power density from each sector can be calculated and allows the SINR to be determined.

5.3 Signal-to-Noise-and-Interference Contours

Let us assume a full-reuse only setup, i.e. all sectors of each site are co-channel interferers.

Figures 5.9a and 5.9b show exemplary SINR maps with constant-SINR contours for the 2-D- and 3-D case. Note that in the 3-D scenario, the area of high SINR within the sector is larger due to the employed electrical downtilt. Thus, by downtilting the antenna, the transmitted signal power is focused more strongly into the corresponding target sector and also interference in

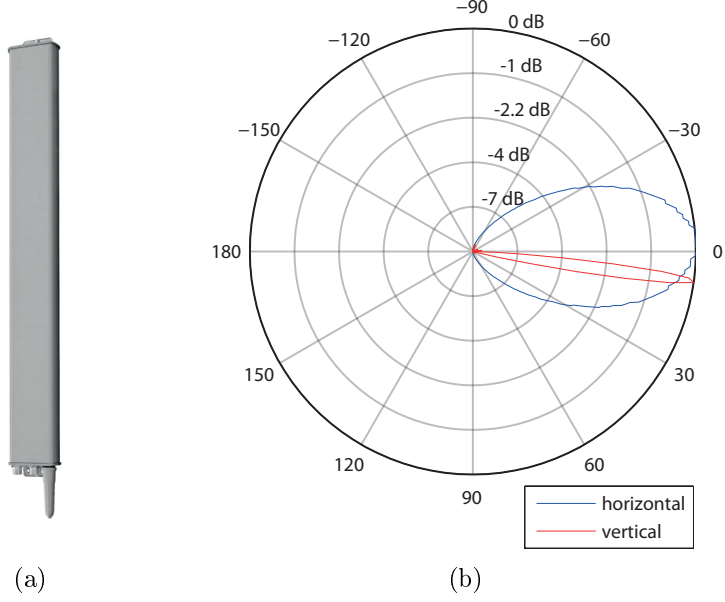


Figure 5.4: (a) Kathrein 742 215 Panel antenna [3], (b) Horizontal- and vertical radiation pattern plotted in logarithmic scale.

the adjacent cells is reduced. This effect can also be observed in Figure 5.8, which shows exemplary SINR ECDF curves for a 2-D- and a 3-D scenario, with dots denoting the average SINR.

Unlike in omnidirectional scenarios, no symmetry is figured out for the SINR contours. Thus, the partitioning boundary ρ , which separates FR- and PR zone in each sector, has an irregular shape. For an FFR scheme with a given ρ , the SINR is then expressed as

$$\gamma_{\rho}(x, y) = \begin{cases} \text{SINR}_{\text{FR}}(x, y), & (x, y) \in \text{FR zone} \\ \text{SINR}_{\text{PR}}(x, y), & (x, y) \in \text{PR zone}. \end{cases} \quad (5.4)$$

As a result of the different SINR contours and the absence of circular symmetry, it is not possible anymore to define the optimal partitioning boundary (ρ^*) as a radius. Thus, the optimization of the FFR partitioning scheme now aims at maximizing average capacity density by finding the optimal partitioning boundary (ρ^*) and normalized FR bandwidth (β_{FR}^*) with respect to the constraints, as formulated in Equation (5.1).

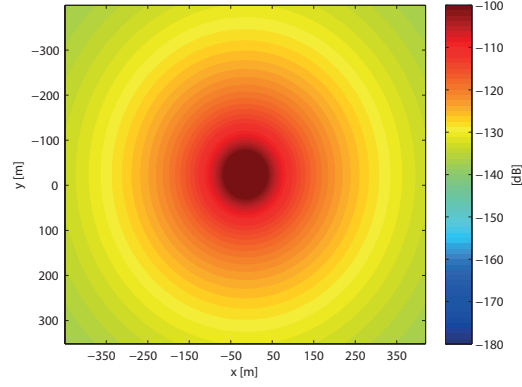


Figure 5.5: Exemplary channel power gain $L(d)|_{\text{dB}}$ using exponential path loss model ($\alpha = 3.6$)

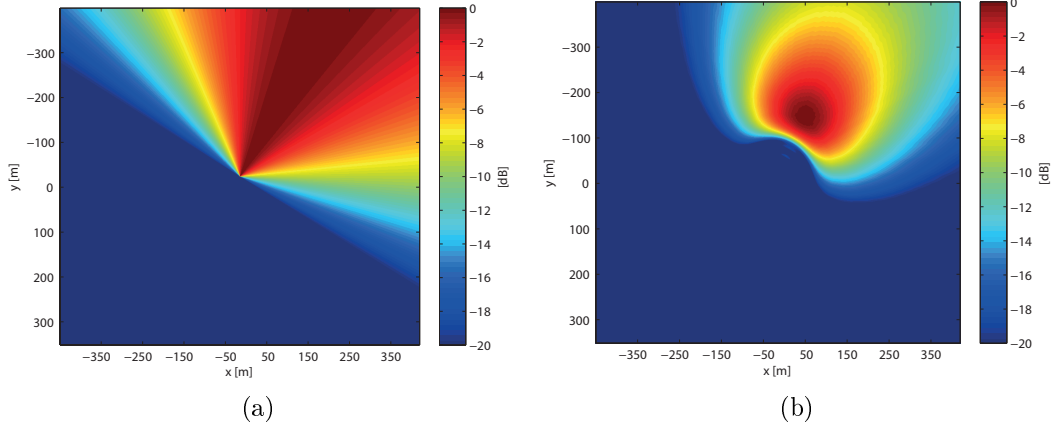


Figure 5.6: Antenna gain $G_{\text{Tx}}(x, y)|_{\text{dB}}$: (a) 2-D (b) 3-D (Antenna electrically downtilted by 8°)

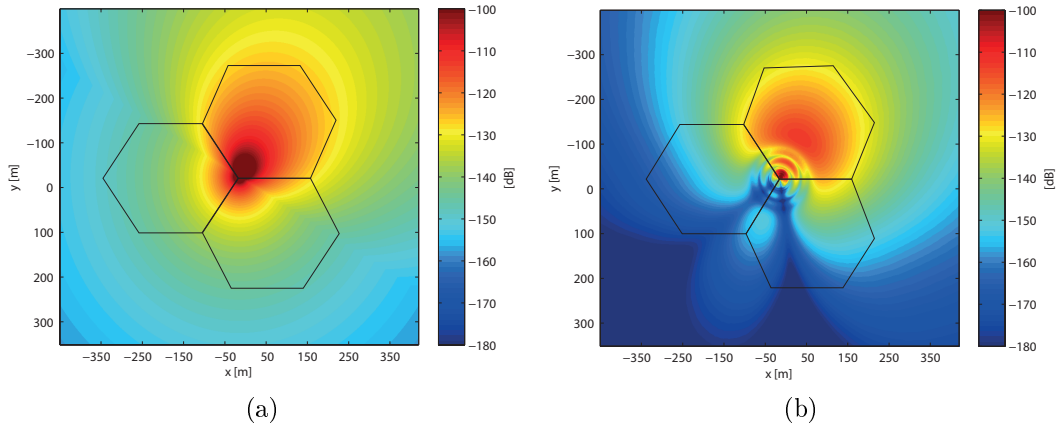


Figure 5.7: Received power density $p_{\text{Rx}}|_{\frac{\text{dBm}}{\text{Hz}}} = p_{\text{Tx}}|_{\frac{\text{dBm}}{\text{Hz}}} + G_{\text{Tx}}|_{\text{dB}} + L|_{\text{dB}}$: (a) 2-D (b) 3-D (Antenna electrically tilted down by 8°)

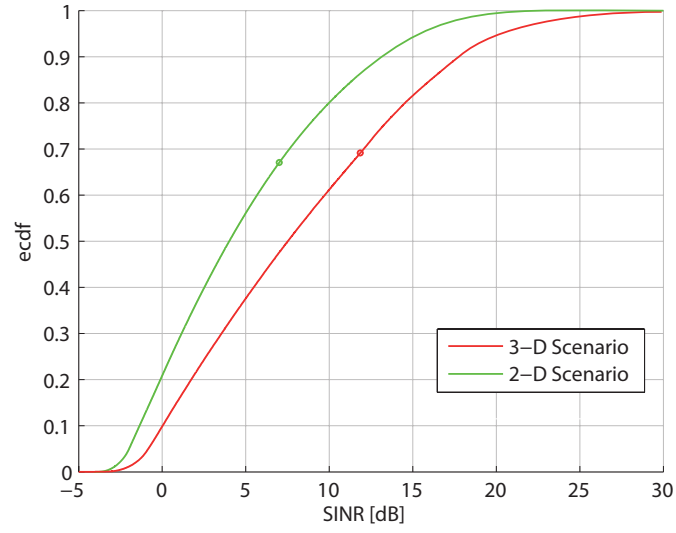


Figure 5.8: SINR ECDF curves for 2-D- and 3-D sectorized scenario (antenna electrically downtilted by 8° in 3-D scenario)

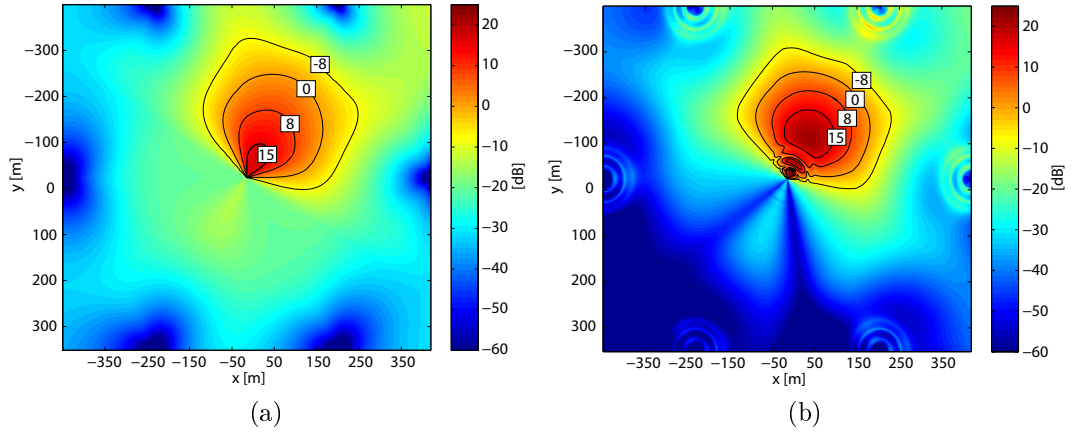


Figure 5.9: SINR map with constant-SINR contours in sectorized scenario: (a) 2-D (b) 3-D (antenna electrically downtilted by 8°)

5.4 Optimization of Sectorized Scenarios

5.4.1 Optimization Proposal

First of all, the *bandwidth density*, defined in Equation (3.10) for the circular symmetric case, is reformulated as

$$b_{\rho, \beta_{\text{FR}}}(x, y) = \begin{cases} \frac{\beta_{\text{FR}}}{A_{\text{FR}}(\rho)}, & (x, y) \in \text{FR zone} \\ \frac{\beta_{\text{PR}}(\beta_{\text{FR}})}{A_{\text{PR}}(\rho)}, & (x, y) \in \text{PR zone}, \end{cases} \quad (5.5)$$

A user at position (x, y) then achieves a *capacity density* (bit/s/Unit of Surface):

$$c_{\rho, \beta_{\text{FR}}}(x, y) = b_{\rho, \beta_{\text{FR}}}(x, y) \log_2 (1 + \gamma_{\rho}(x, y)), \quad (5.6)$$

where $\gamma_{\rho}(x, y)$ denotes the SINR at position (x, y) . With the SINR expression from Equation (5.4), Equation (5.6) can be rewritten as:

$$c_{\rho, \beta_{\text{FR}}}(x, y) = \begin{cases} c_{\text{FR}, \rho, \beta_{\text{FR}}}(x, y), & (x, y) \in \text{FR zone} \\ c_{\text{PR}, \rho, \beta_{\text{PR}}}(x, y), & (x, y) \in \text{PR zone}, \end{cases} \quad (5.7)$$

where

$$c_{\text{FR}, \rho, \beta_{\text{FR}}}(x, y) = \frac{\beta_{\text{FR}}}{A_{\text{FR}}(\rho)} \log_2 (1 + \text{SINR}_{\text{FR}}(x, y)), \quad (5.8)$$

$$c_{\text{PR}, \rho, \beta_{\text{PR}}}(x, y) = \frac{\beta_{\text{PR}}(\beta_{\text{FR}})}{A_{\text{PR}}(\rho)} \log_2 (1 + \text{SINR}_{\text{PR}}(x, y)). \quad (5.9)$$

A given user is either allocated to an FR- or PR zone, according to where the capacity density is higher, i.e.

$$c_{\text{FFR}, \rho, \beta_{\text{FR}}}(x, y) = \max (c_{\text{FR}, \rho, \beta_{\text{FR}}}(x, y), c_{\text{PR}, \rho, \beta_{\text{PR}}}(x, y)) \quad (5.10)$$

Then the partitioning boundary (ρ) for each sector is calculated as

$$\rho = \{(x, y) | c_{\text{FR}, \rho, \beta_{\text{FR}}}(x, y) = c_{\text{PR}, \rho, \beta_{\text{PR}}}(x, y)\} \quad (5.11)$$

5.4.2 Average Capacity Density

In sectorized scenarios, each sector employs an FR- and PR zone, as depicted in Figure 5.1a. A sector's average capacity density is calculated as

$$\bar{c}_s(\rho, \beta_{\text{FR}}) = \frac{1}{A_{\text{sector},s}} \left[\iint_{\mathcal{A}_{\text{FR},s}(\rho)} c_{\text{FR},\rho,\beta_{\text{FR}}}(x,y) dx dy + \iint_{\mathcal{A}_{\text{PR},s}(\rho)} c_{\text{PR},\rho,\beta_{\text{FR}}}(x,y) dx dy \right], \quad (5.12)$$

where s denotes the sector number¹ and $c_{\text{FR},\rho,\beta_{\text{FR}}}(x,y)$ and $c_{\text{PR},\rho,\beta_{\text{FR}}}(x,y)$ are capacity densities, as referred from Equations (5.8) and (5.9). The sector area $A_{\text{sector},s}$ is calculated as $A_{\text{sector},s} = A_{\text{FR},s}(\rho) + A_{\text{PR},s}(\rho)$, with $A_{\text{FR},s}(\rho)$ and $A_{\text{PR},s}(\rho)$ denoting the areas of the FR- and PR zone.

Then, the average capacity density in a cell with N_{sectors} sectors is expressed as

$$\bar{c}(\rho, \beta_{\text{FR}}) = \frac{1}{N_{\text{sectors}}} \sum_s \bar{c}_s(\rho, \beta_{\text{FR}}) \quad (5.13)$$

Note that, since the same antenna radiation pattern is used for each sector and the main radiation directions are equally spaced at an angle of 120° , $\bar{c}(\rho, \beta_{\text{FR}}) = \bar{c}_s(\rho, \beta_{\text{FR}})$ holds. In this work, however, the generalized notation is kept.

¹Each sector of a site is labeled by a sector number, as shown in Figure 5.1a

Chapter 6

Simulation Results of Sectorized Scenarios

6.1 Simulation Setup and Calculation Methods

6.1.1 Assumptions and Simulation Parameters

Now, FFR optimization in sectorized scenarios, as formulated in Equation (5.1) is investigated by simulations. Thereto, a cluster of equidistantly spaced sites, each equipped with three sector antennas, is used, as depicted in Figure 6.1.

The following assumptions have been made:

- A hexagonal grid of sites with a center cell (BS_0) surrounded by six direct neighbors ($BS_1 \dots BS_7$), as shown in Figure 6.1
- Each site is equipped with three sector antennas. The main radiation directions are equally spaced at an angle of 120°
- Each sector has an FR zone using $FRF = 1$ and a PR zone using $FRF = 3$
- A worst-case interference situation, i.e. all interfering BSs are transmitting at maximum available power

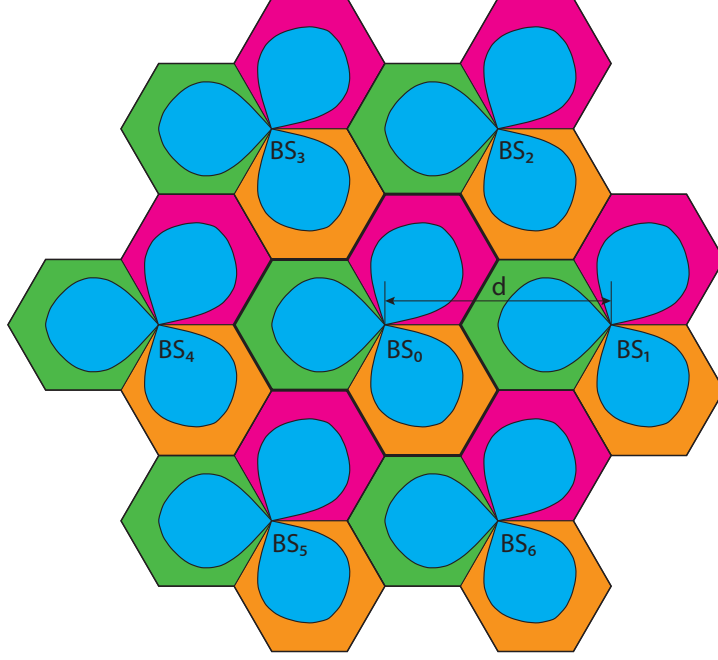


Figure 6.1: Cell grid of sectorized scenario. FR zones depicted in blue. PR zones depicting the employed reuse-3 scheme

- Constant user-density within the cells

Results are evaluated in the center cell (BS_0), while the surrounding sites serve as interferers.

Both 2-D- and 3-D scenarios are investigated. In the 2-D case, the scenario is restricted to a flat horizontal plane, whereas in the 3-D case, transmitter- (h_{Tx}) and receiver height (h_{Rx}) are also taken into account, as shown in Figure 5.2. Table 6.1 provides the simulation parameters for both scenarios.

FFR performance is compared to the performance of a conventional reuse-

Inter-site distance d	433	m
Total bandwidth B_{TOT}	5	MHz
Center frequency f_c	2	GHz
Noise spectral density N_0	-174	dBm
Path loss exponent α	3.6	-
Total power P_{TOT}	20	W

Table 6.1: Simulation parameters of sectorized scenarios

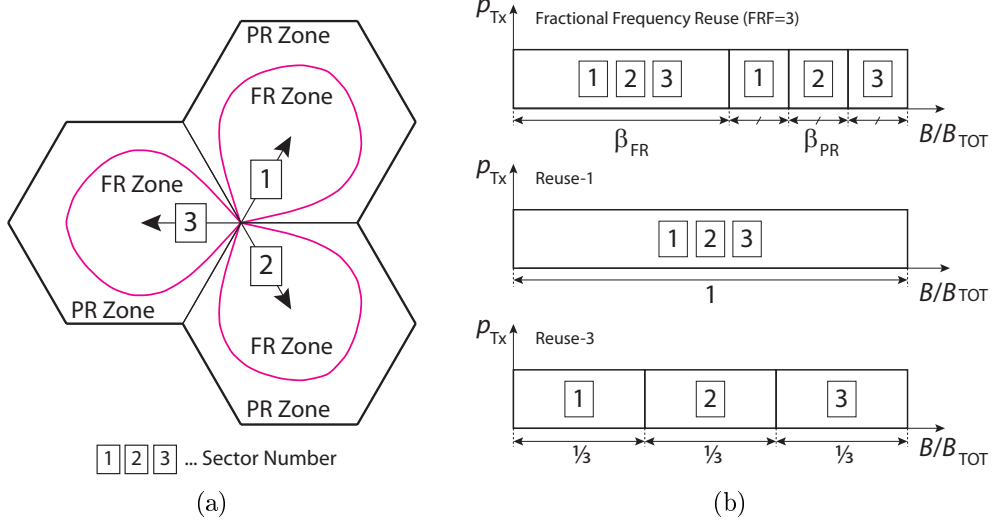


Figure 6.2: (a) Cell with three sectors (b) Bandwidth allocation of FFR, reuse-1 and reuse-3

1- (FRF = 1) and reuse-3 scheme (FRF = 3). Both conventional schemes apply the simulation parameters given in Table 6.1 and the cell cluster shown in Figure 6.1. In order to ensure the same cell size as in the omnidirectional scenario, an inter-site distance of 433 m has been chosen (i.e. $2 \cdot \frac{\sqrt{3}}{2} 250$ m, see Table 4.1 and Figure 4.1).

Figure 6.2 depicts the bandwidth allocation of the two schemes together with FFR.

6.1.2 Calculation Methods

In sectorized scenarios, average capacity density is determined by the mean of the average sector capacity densities (Equation (5.13)). This is done in MATLAB by first calculating the average sector capacity densities of reuse-1, reuse-3 and FFR as

$$\bar{c}_{s,\text{Reuse-1}} = \frac{1}{\#\text{sector},s} \sum_{\mathcal{A}_{\text{cell}}} \frac{B_{\text{TOT}}}{\#\text{sector},s a_{\text{pp}}} \log_2 (1 + \text{SINR}_{\text{FRF1}}) \quad (6.1)$$

$$\bar{c}_{s,\text{Reuse-3}} = \frac{1}{\#\text{sector},s} \sum_{\mathcal{A}_{\text{cell}}} \frac{1}{3} \frac{B_{\text{TOT}}}{\#\text{sector},s a_{\text{pp}}} \log_2 (1 + \text{SINR}_{\text{FRF3}}) \quad (6.2)$$

$$\begin{aligned} \bar{c}_{s,\text{FFR}}(\rho, \beta_{\text{FR}}) = \frac{1}{\#\text{sector},s} & \left[\sum_{\mathcal{A}_{\text{FR},s}(\rho)} \frac{\beta_{\text{FR}} B_{\text{TOT}}}{\#\text{FR},s(\rho) a_{\text{pp}}} \log_2 (1 + \text{SINR}_{\text{FRF1}}) \right. \\ & \left. + \sum_{\mathcal{A}_{\text{PR},s}(\rho)} \frac{1 - \beta_{\text{FR}}}{3} \frac{B_{\text{TOT}}}{\#\text{PR},s(\rho) a_{\text{pp}}} \log_2 (1 + \text{SINR}_{\text{FRF3}}) \right], \end{aligned} \quad (6.3)$$

where s is the sector number, a_{pp} is the pixel size (m^2/pixel), \mathcal{A} denotes a region and $\#$ the number of pixels within. Then, the average capacity densities in a cell of N_{sectors} sectors are obtained as

$$\bar{c}_{\text{Reuse-1}} = \frac{1}{N_{\text{sectors}}} \sum_s \bar{c}_{s,\text{Reuse-1}} \quad (6.4)$$

$$\bar{c}_{\text{Reuse-3}} = \frac{1}{N_{\text{sectors}}} \sum_s \bar{c}_{s,\text{Reuse-3}} \quad (6.5)$$

$$\bar{c}_{\text{FFR}}(\rho, \beta_{\text{FR}}) = \frac{1}{N_{\text{sectors}}} \sum_s \bar{c}_{s,\text{FFR}}(\rho, \beta_{\text{FR}}). \quad (6.6)$$

6.2 Simulation Results of Two-dimensional Scenarios

In simulations in which a 2-D antenna radiation pattern is employed, the scenario is restricted to a flat plane (see Figure 5.2). The cell cluster is composed of a center site (BS_0) and six direct neighbors ($\text{BS}_1 \dots \text{BS}_7$), as depicted in Figure 6.1, where each site is equipped with three sector antennas that sectorize the cell.

In this simulation, the sector antenna introduced in Section 5.2.2 is employed. Figure 5.3 depicts its horizontal radiation pattern as referred from the stan-

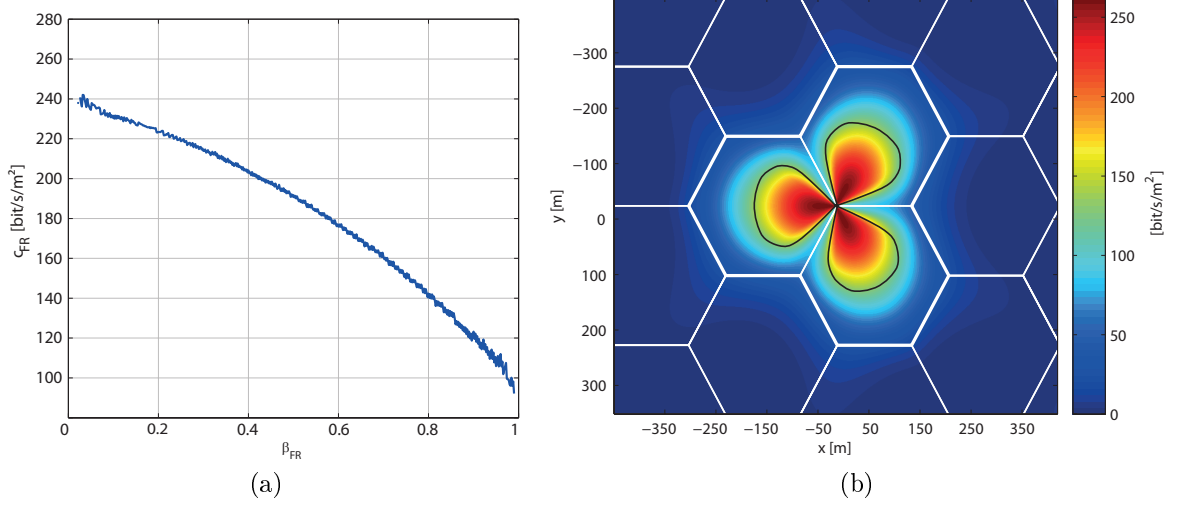


Figure 6.3: (a) Capacity density switching point: $c_{FR,\rho,\beta_{FR}}(x,y) = c_{PR,\rho,\beta_{FR}}(x,y)$ in 2-D sectorized scenario (b) Capacity density map $c_{FR,\rho,\beta_{FR}}(x,y)$ for $\beta_{FR} = 0.75$. Partitioning boundary (ρ) depicted as black line.

dard [2].

Let us begin with the partitioning boundary ρ . According to Equation (5.11), ρ is found along (x,y) , where the FR- and PR capacity densities are equal:

$$c_{FR,\rho,\beta_{FR}}(x,y) = c_{PR,\rho,\beta_{FR}}(x,y), \quad (x,y) \in \rho. \quad (6.7)$$

Figure 6.3a depicts the simulation result for $c_{FR,\rho,\beta_{FR}}(x,y)$ for the possible range of β_{FR} . Thus, it shows the capacity density value along the partitioning boundary for a given β_{FR} . An exemplary partitioning boundary is plotted as a black line in the capacity density map in Figure 6.3b.

Then, the average-, cell-edge and peak capacity densities are obtained, as shown in Figures 6.4a–6.4c. It is seen that the proposed FFR scheme outperforms reuse-1 in terms of average capacity density for $\beta_{FR} > 0.4$ and reuse-3 in terms of cell-edge capacity for $\beta_{FR} < 0.62$. The labels mark the points where FFR achieves no average performance loss compared to reuse-1, reuse-3 equivalent cell-edge performance and maximum average capacity density: $\beta_{FR} = 0.40$, $\beta_{FR} = 0.62$ and $\beta_{FR} = 0.75$ respectively.

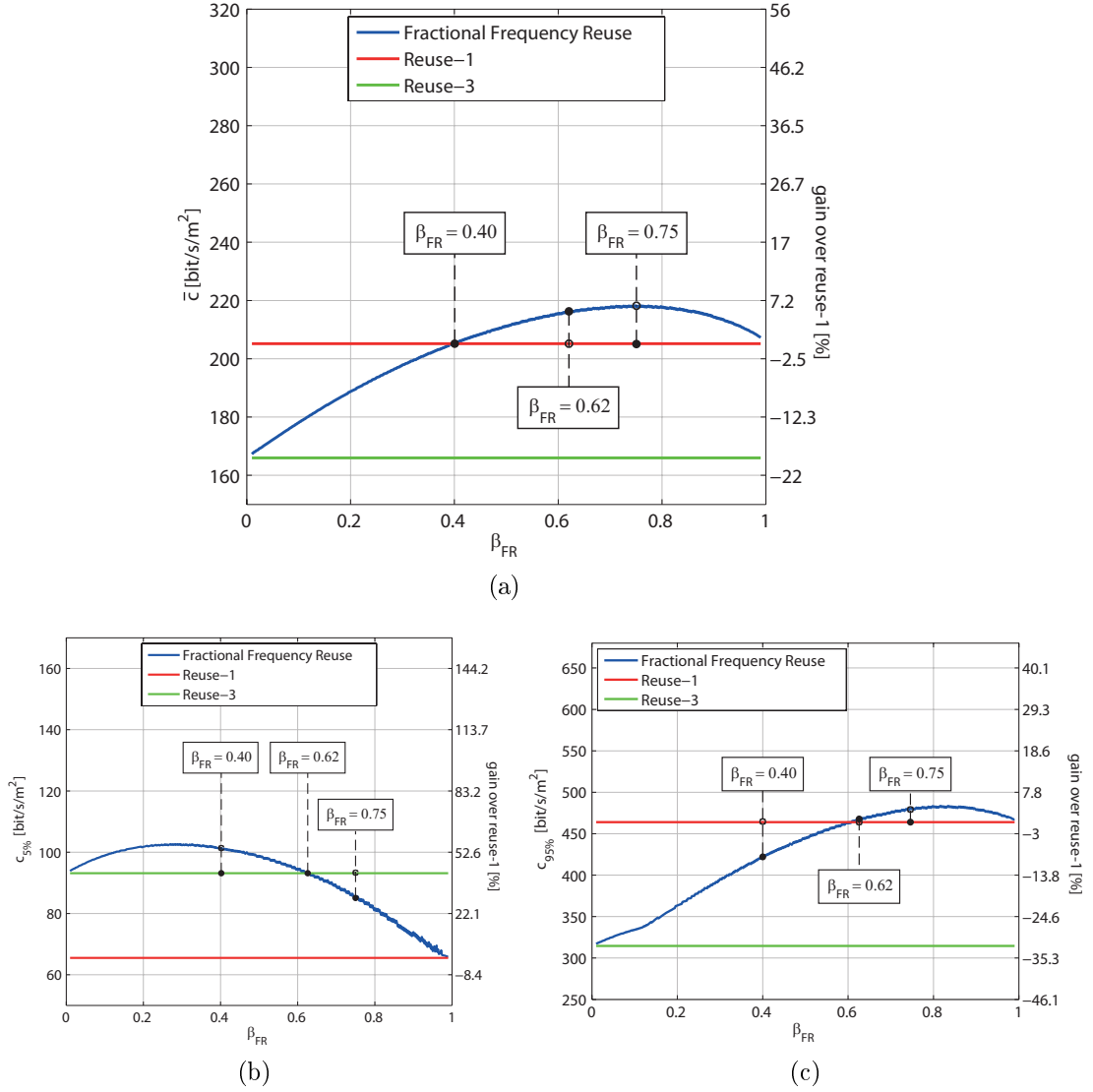


Figure 6.4: (a) Average capacity densities, (b) cell-edge capacities and (c) peak capacities in 2-D sectorized scenario. FFR depicted in blue. Red and green lines depicting reuse-1 and reuse-3. Labels denoting points, where FFR achieves no average performance loss compared to reuse-1 ($\beta_{FR} = 0.40$), reuse-3 equivalent cell-edge performance ($\beta_{FR} = 0.62$) and maximum average capacity density ($\beta_{FR} = 0.75$).

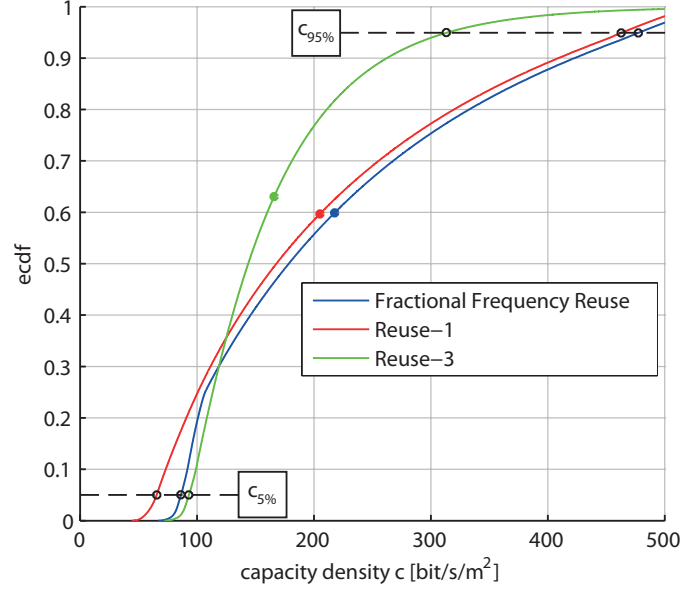


Figure 6.5: Capacity density ECDF curves for $\beta_{\text{FR}} = 0.75$ in 2-D sectorized scenario, FFR depicted in blue. Red and green curves depict reuse-1 and reuse-3 respectively.

Let us investigate on $\beta_{\text{FR}} = 0.75$, where the scheme achieves maximum average capacity density. Figure 6.5 shows the capacity density ECDF curves for this specific bandwidth allocation, with dots denoting the average capacity densities of FFR (blue), reuse-1 (red) and reuse-3 (green). Note that FFR has a slightly higher peak performance than reuse-1, while its cell-edge performance is comparable to reuse-3. Its peak capacity, however, clearly exceeds reuse-3 (see Figure 6.4c).

Figure 6.6 now shows the relative capacity density gains of FFR, compared to a reuse-1 scheme. The maximum achievable gain in terms of average capacity density \bar{c} will depend on how restrictive the edge performance constraint c_1 is set relative to the total bandwidth, which is 5 MHz in the simulations. Table 6.2 provides simulation results at significant values, where FFR achieves:

- Maximum average capacity density (\bar{c}_{max})
- Reuse-3 equivalent performance at cell edge ($c_{5\%}$)

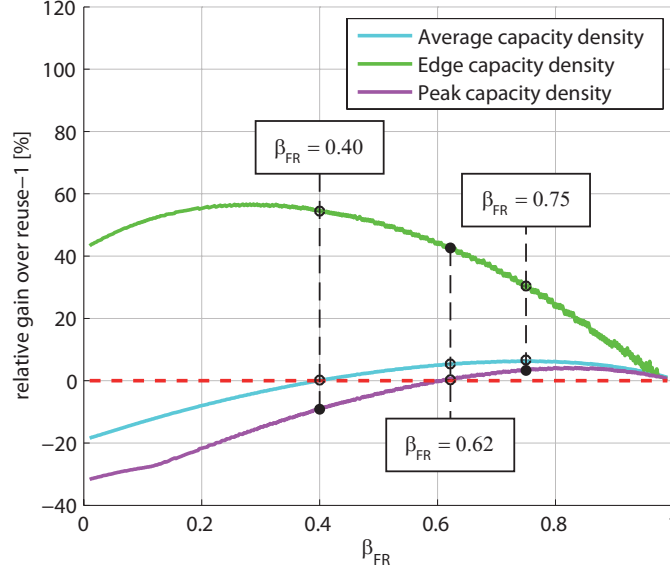


Figure 6.6: Relative capacity density gains of FFR over reuse-1 scheme in 2-D sectorized scenario

- No loss in average capacity density (\bar{c}) compared to reuse-1
- No loss in peak capacity ($c_{95\%}$) compared to reuse-1

Without the cell-edge constraint, the maximum average capacity density is achieved at $\beta_{FR} = 0.75$, where FFR outperforms reuse-1 by 6.37% in terms of average performance (\bar{c}), 29.97% in edge capacity ($c_{5\%}$) and 3.64% in peak capacity ($c_{95\%}$).

Results show that the proposed FFR scheme outperforms conventional schemes not only in omnidirectional- but also in 2-D sectorized scenarios. In the next section, results from a sectorized layout, using 3-D antenna radiation patterns, are shown.

6.3 Simulation Results of Three-dimensional Scenarios

The 2-D scenario is extended to 3-D by additionally considering transmitter- and receiver height, as well as a vertical radiation pattern, as shown in

		Gain over reuse-1 [%]			β_{FR}
		$c_{5\%}$	\bar{c}	$c_{95\%}$	
(1)	$\bar{c}_{\text{max}} = \max_{\rho, \beta_{\text{FR}}} \bar{c}_{\text{FFR}}(\rho, \beta_{\text{FR}})$	29.97%	6.37%	3.64%	0.75
(2)	$c_{5\%, \text{FFR}} = c_{5\%, \text{Reuse-3}}$	41.97%	5.41%	0.74%	0.62
(3)	$\bar{c}_{\text{FFR}} = \bar{c}_{\text{Reuse-1}}$	54.46%	0.00%	-9.03%	0.40
(4)	$c_{95\%, \text{FFR}} = c_{95\%, \text{Reuse-1}}$	43.72%	5.08%	0.00%	0.60

- (1) optimized FFR, \bar{c} maximized (3) no average loss
(2) reuse-3 performance at cell-edge (4) no peak loss

Table 6.2: Relative gains of FFR scheme over reuse-1 at significant bandwidth allocations (β_{FR}) in 2-D sectorized scenario

Figure 5.2. Thereto, the cell cluster depicted in Figure 6.1 is reused.

For simulations of the 3-D case, however, it is assumed that each site is equipped with three Kathrein 742215 sector antennas, as introduced in Section 5.2.3. Figure 5.4b shows the antenna's horizontal- and vertical gain pattern.

Simulations are carried out for a transmitter height $h_{\text{Tx}} = 20$ m and a receiver height $h_{\text{Rx}} = 1.5$ m. Furthermore, all antennas are assumed to be electrically downtilted by 8° .

First, the partitioning boundary (ρ), as defined in Equation (5.11), is investigated. Figure 6.7 shows the simulation-obtained optimum switching point (see Equation (6.7)), where $c_{\text{FR}, \rho, \beta_{\text{FR}}}(x, y) = c_{\text{PR}, \rho, \beta_{\text{FR}}}(x, y)$. Exemplary partitioning boundaries are depicted as black lines in Figure 6.8.

Then, the average capacity densities and cell-edge capacities are obtained, as shown in Figures 6.9a and 6.9b, where FFR is depicted in blue and the red and green lines depict reuse-1 and reuse-3 respectively.

It is seen that the proposed FFR scheme achieves higher average capacity density than reuse-1 for $\beta_{\text{FR}} > 0.4$ and higher cell-edge capacity than reuse-3 for $\beta_{\text{FR}} < 0.66$. The scheme's relative capacity density gains compared to reuse-1 are depicted in Figure 6.10, and Table 6.3 provides the exact values for significant constraints.

Without restricting the cell-edge performance ($c_{5\%}$), FFRs maximum average capacity density is obtained at $\beta_{\text{FR}} = 0.75$ (the same point as for the

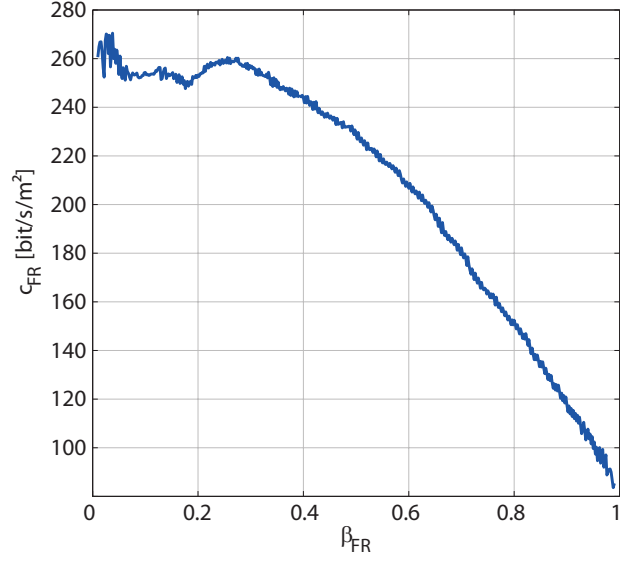


Figure 6.7: Capacity density switching point: $c_{\text{FR},\rho,\beta_{\text{FR}}}(x,y) = c_{\text{PR},\rho,\beta_{\text{FR}}}(x,y)$ in 3-D sectorized scenario

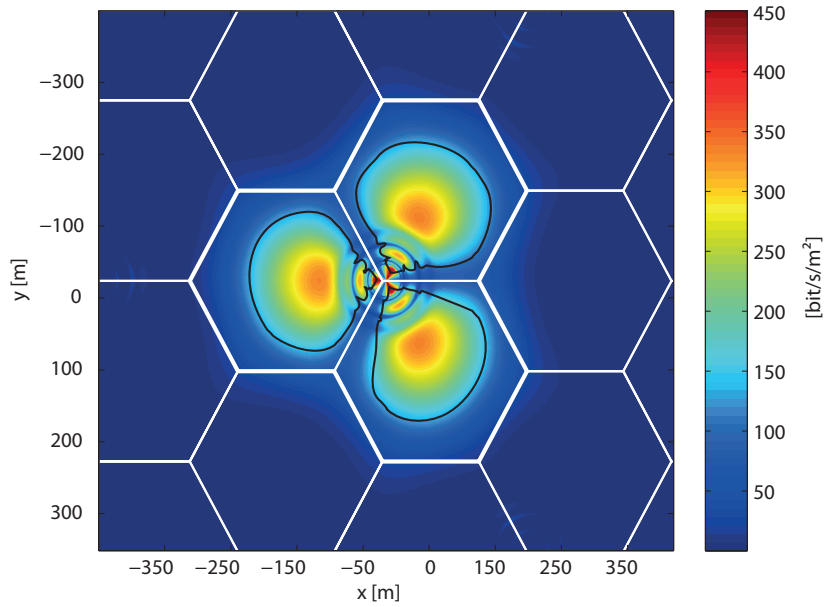


Figure 6.8: Capacity density map in 3-D sectorized scenario. Black lines depict partitioning boundaries (ρ) at $\beta_{\text{FR}} = 0.75$.

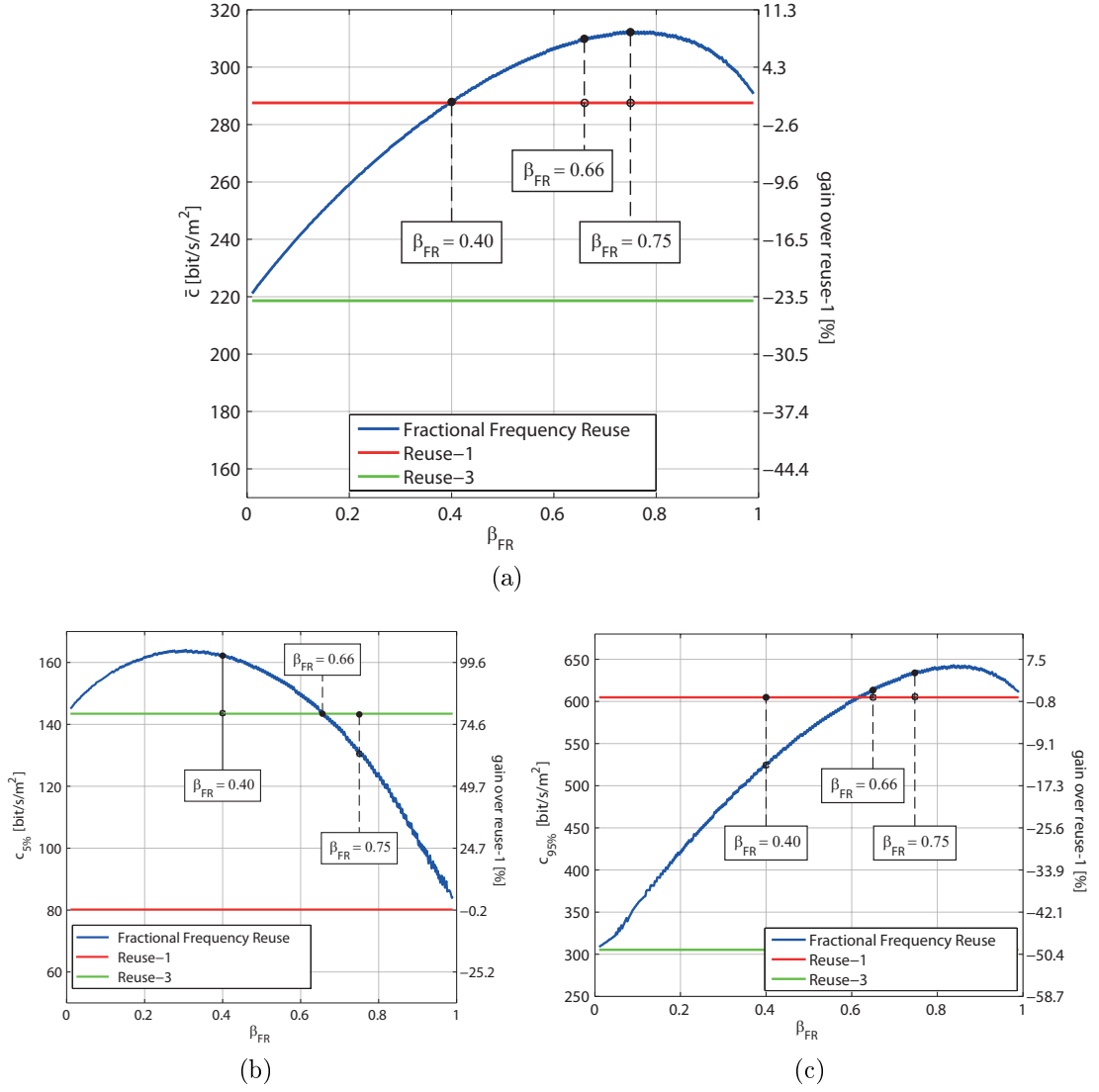


Figure 6.9: (a) Average capacity densities, (b) cell-edge capacities and (c) peak capacities in 3-D sectorized scenario. FFR depicted in blue. Red and green lines depicting reuse-1 and reuse-3. Labels denoting points, where FFR achieves no average performance loss compared to reuse-1 ($\beta_{\text{FR}} = 0.40$), reuse-3 equivalent cell-edge performance ($\beta_{\text{FR}} = 0.66$) and maximum average capacity density ($\beta_{\text{FR}} = 0.75$).

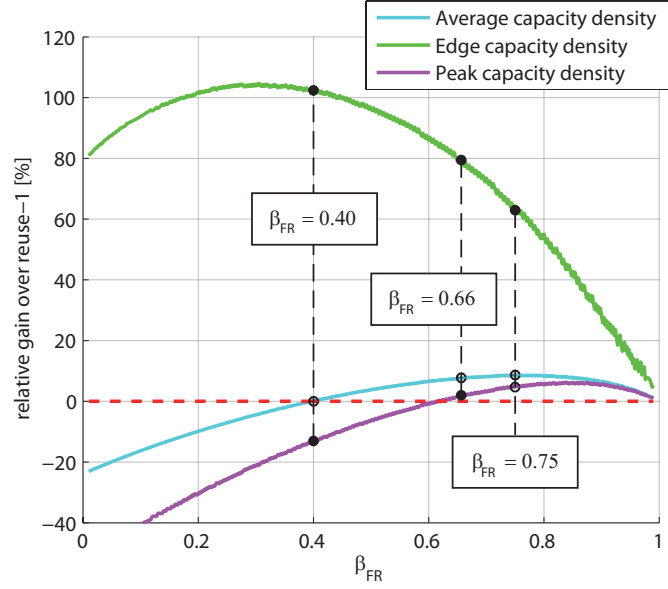


Figure 6.10: Relative capacity density gains of FFR over reuse-1 scheme in 3-D sectorized scenario

	Gain over reuse-1 [%]			β_{FR}
	$c_{5\%}$	\bar{c}	$c_{95\%}$	
(1) $\bar{c}_{\max} = \max_{\rho, \beta_{FR}} \bar{c}_{FFR}(\rho, \beta_{FR})$	61.81%	8.68%	5.21%	0.75
(2) $c_{5\%, FFR} = c_{5\%, Reuse-3}$	78.33%	7.79%	2.03%	0.66
(3) $\bar{c}_{FFR} = \bar{c}_{Reuse-1}$	102.30%	0.00%	-13.19%	0.40
(4) $c_{95\%, FFR} = c_{95\%, Reuse-1}$	84.59%	6.91%	0.00%	0.61

- | | |
|--|---------------------|
| (1) optimized FFR, \bar{c} maximized | (3) no average loss |
| (2) reuse-3 performance at cell-edge | (4) no peak loss |

Table 6.3: Relative gains of FFR scheme over reuse-1 at significant bandwidth allocations (β_{FR}) in 3-D sectorized scenario

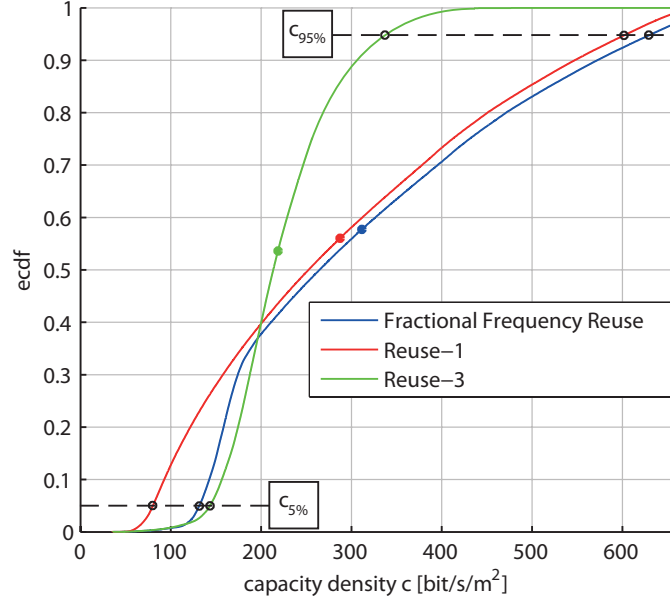


Figure 6.11: Capacity-density ECDF for $\beta_{\text{FR}} = 0.75$ in 3-D sectorized scenario, FFR depicted in blue. Red and green curves depict reuse-1 and reuse-3 respectively.

2-D case) and exceeds reuse-1 by 8.68%. For this specific bandwidth allocation, Figure 6.11 depicts the capacity density ECDF curves of FFR (blue), reuse-1 (red) and reuse-3 (green). A behaviour similar to the 2-D scenario is observed. While the FFR scheme outperforms reuse-1 in peak capacity by 4.66%, its edge capacity is comparable to reuse-3 and exceeds reuse-1 by 64.23%.

Now, demanding at least reuse-3 performance at cell-edge (i.e. $c_{5\%} \geq c_1$, where c_1 is the cell-edge capacity of a reuse-3 scheme), a maximum gain of 7.79% in average capacity density (\bar{c}) is achieved.

Thus, the proposed scheme can effectively be applied in 3-D sectorized scenarios. The impact of electrically downtilting the antennas is left over to the last section of this chapter.

6.4 Optimization Results

Let us discuss simulation results of the 2-D- and 3-D scenario in terms of the formulated optimization problem (Equation (5.1)), which constrains maximization of average capacity density (\bar{c}) by demanding a minimum cell-edge performance ($c_{5\%}$).

Without this constraint, the maximum average capacity density \bar{c}_{\max} ¹ is achieved at $\beta_{\text{FR}} = 0.75$ in both scenarios. For this specific bandwidth allocation, FFR outperforms a reuse-1 scheme in \bar{c} by 6.37% in a 2-D- and by 8.43% in a 3-D scenario (see Figure 6.12a).

Despite the similarity of the relative gains, the corresponding \bar{c} values are considerably different. While a maximum average capacity density $\bar{c}_{\max} = 218$ bit/s/m² is achieved in the 2-D case, $\bar{c}_{\max} = 313$ bit/s/m² are obtained in the 3-D case (see Figure 6.12b). A remarkable difference is also present for the performance at cell-edge ($c_{5\%}$): 84.94 bit/s/m² in a 2-D- and 131.66 bit/s/m² in a 3-D scenario (see Figure 6.12c).

This is caused by electrically downtilting the sector antennas in the 3-D case. Thereby, the transmit power of the useful signal is focused into the target sector and interference in adjacent cells is reduced (see Section 5.3).

Now, constraining FFR to perform equally or better than a reuse-3 scheme at cell-edge, i.e. $c_{5\%} \geq c_1$, where c_1 is the cell-edge capacity of reuse-3, optimization results are obtained as follows:

The restriction is met for $\beta_{\text{FR}} < 0.62$ (2-D case, see Figure 6.4b) and $\beta_{\text{FR}} < 0.66$ (3-D case, see Figure 6.9b). The constrained FFR scheme achieves $\bar{c}_{\max} = 216.27$ bit/s/m² in a 2-D- and $\bar{c}_{\max} = 309.88$ bit/s/m² in a 3-D sectorized scenario (corresponding to gains of 5.41% and 7.76% over reuse-1 in terms of average capacity density). At cell-edge, capacity densities are obtained as $c_{5\%} = 93.01$ bit/s/m² (41.97% over reuse-1) in the 2-D- and $c_{5\%} = 142.24$ bit/s/m² (78.33% over reuse-1) in the 3-D case. Again, the effect of electrically downtilting the antennas is not only a higher capacity density but also a higher gain in relative terms due to using FFR.

¹ $\bar{c}_{\max} = \max_{\rho, \beta_{\text{FR}}} \bar{c}(\rho, \beta_{\text{FR}})$

Thus, the proposed FFR scheme can effectively be applied in sectorized scenarios to maximize average capacity density while complying a minimum capacity demand at cell-edge. Electrical downtilting, a common practice in today's real systems, even increases the FFR scheme's optimal performance.

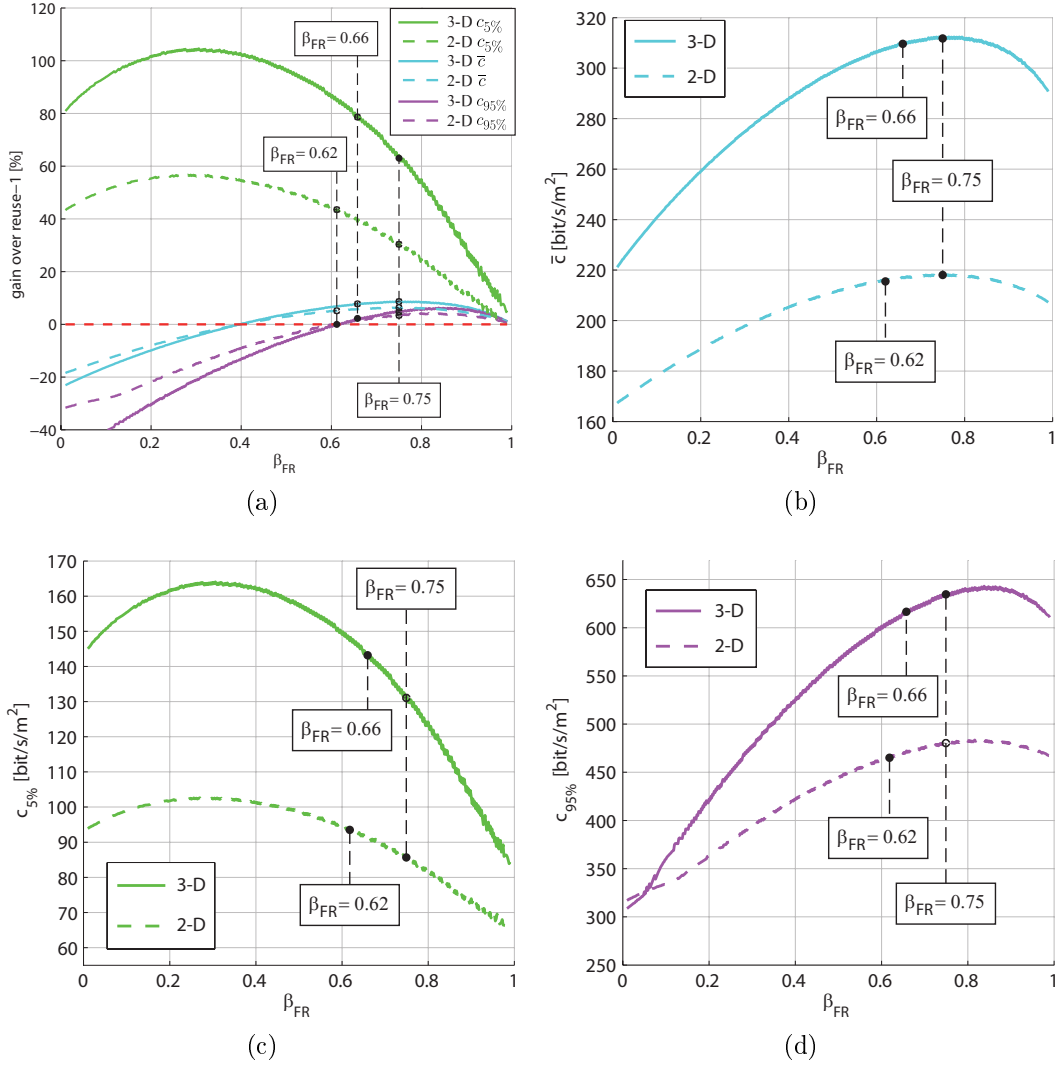


Figure 6.12: Comparison of simulation results for 2-D- and 3-D sectorized scenarios: (a) Relative capacity density gains over reuse-1, (b) average capacity density ($bit/s/m^2$), (c) cell-edge capacity ($bit/s/m^2$) and (d) peak capacity ($bit/s/m^2$)

Chapter 7

Conclusion and Outlook

In this work, an optimized FFR partitioning scheme was proposed and analyzed. It aims at maximizing the average capacity density (analogous to the concept of per-user throughput) while maintaining a minimum capacity at cell-edge (analogous to ensuring a minimum edge user throughput).

For the scheme's optimization, an analytical model was formulated, assuming static scenarios with constant uniform user distribution. Numerical evaluations illustrate the capacity variations and confirm the existence of an optimal solution.

First, the effectiveness of the proposed FFR scheme was verified in omnidirectional scenarios by comparison with a conventional reuse-1- and reuse-3 scheme. However, the common assumption of a noise limited reuse-3 scheme critically alters the results and was shown to be not realistic. Therefore, interference limitation in both the FR- and PR zones was assumed.

Simulation results show that, with properly allocated bandwidth, FFR outperforms the conventional reuse-1 scheme in terms of average- and peak capacity density, while achieving a cell-edge performance comparable to the conventional reuse-3 scheme.

Having proven the validity in omnidirectional scenarios, the effectiveness of FFR has also been shown for the, less analytically treatable, sectorized case. First, simulation results for a 2-D layout verified its effective applicability. By considering transmitter- and receiver height, the scenario was then extended

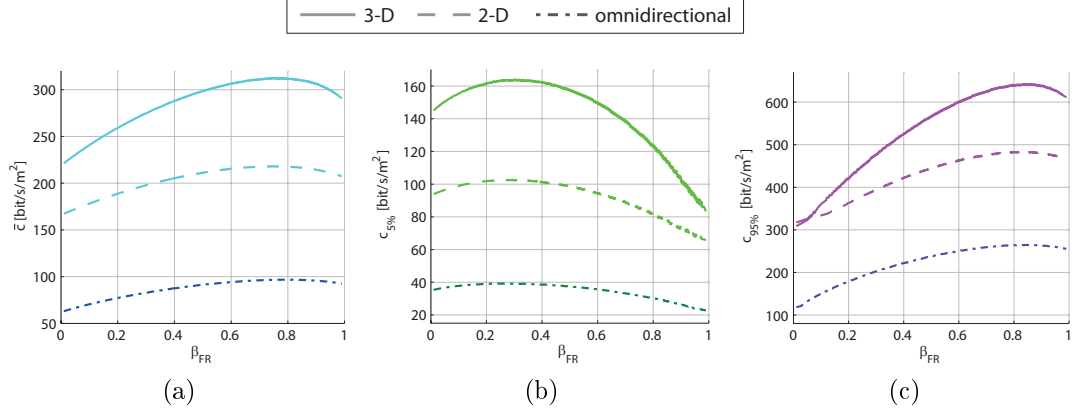


Figure 7.1: Simulation results of (a) average capacity densities \bar{c} , (b) edge capacity densities ($c_{5\%}$) and (c) peak capacity densities ($c_{95\%}$) in 2-D-, 3-D- and omnidirectional scenarios

to 3-D. For both sectorized scenarios, results show that FFR achieves higher average- and peak capacity densities than a reuse-1 scheme, even when demanding a reuse-3 scheme's performance at cell-edge.

The 3-D setup further allowed to investigate on the effect of electrically tilting the sector antennas. Due to the more optimal SINR distribution, a significant gain in average-, edge- and peak performance compared to omnidirectional- and non-tilted 2-D scenarios is shown (both relative and absolute). This performance improvement is schematically depicted in Figure 7.1.

In order for the proposed FFR technique to be effectively employed, knowledge about the user's position (x, y) within the cell is required, as well as detailed path loss distributions, which is not covered in this work.

The proposed FFR partitioning exploits the scarce spectral resource more efficiently than conventional schemes (i.e. reuse-1 and reuse-3), in terms of both average and cell-edge performance, thus improving the efficiency with which the limited amount of available bandwidth is employed.

Appendix A

Acronyms

FFR	Fractional Frequency Reuse
ICI	Inter-cell Interference
FR	Full Reuse
PR	Partial Reuse
CCI	Co-Channel Interference
FRF	Frequency Reuse Factor
SINR	Signal-to-Interference-plus-Noise Ratio
bit/s	Bits per Second
ECDF	Empirical Cumulative Distribution Function
BS	Base Station
SNR	Signal-to-Noise Ratio
3-D	Three-dimensional
2-D	Two-dimensional

Bibliography

- [1] A. Alsawah and I. Fijalkow, “**Optimal frequency-reuse partitioning for ubiquitous coverage in cellular systems,**” in *15th European Signal Processing Conference (EUSIPCO)*, 2008. [Online]. Available: <http://publi-etis.ensea.fr/2008/AF08a>
- [2] 3GPP, “**Evolved universal terrestrial radio access (E-UTRA); radio frequency (RF) system scenarios,**” 3rd Generation Partnership Project (3GPP), TS 36.942, May 2009. [Online]. Available: <http://www.3gpp.org/ftp/Specs/html-info/36942.htm>
- [3] Kathrein-Werke KG, “**Kathrein scala division - 742 215 65° panel antenna.**” [Online]. Available: <http://www.kathrein-scala.com/catalog/742215.pdf>
- [4] 3GPP, “**Evolved universal terrestrial radio access (E-UTRA); further advancements for E-UTRA physical layer aspects,**” 3rd Generation Partnership Project (3GPP), TS 36.814, March 2010. [Online]. Available: <http://www.3gpp.org/ftp/Specs/html-info/36814.htm>
- [5] C. Lei and Y. Di, “**Generalized frequency reuse schemes for OFDMA networks: Optimization and comparison,**” in *IEEE 71st Vehicular Technology Conference (VTC 2010-Spring)*, pp. 1 –5, May 2010.
- [6] M. Rahman and H. Yanikomeroglu, “**Enhancing cell-edge performance: a downlink dynamic interference avoidance scheme with inter-cell coordination,**” *IEEE Transactions on Wireless Communications*, vol. 9, no. 4, pp. 1414 –1425, April 2010.

- [7] A. Simonsson, “**Frequency reuse and intercell interference coordination in E-UTRA**,” in *IEEE 65th Vehicular Technology Conference (VTC 2007-Spring)*, pp. 3091 –3095, April 2007.
- [8] Z. Xie and B. Walke, “**Frequency reuse techniques for attaining both coverage and high spectral efficiency in OFDMA cellular systems**,” in *IEEE Wireless Communications and Networking Conference (WCNC 2010)*, pp. 1 –6, April 2010.
- [9] A. Boustani, S. Khorsandi, R. Danesfahani, and N. MirMotahhary, “**An efficient frequency reuse scheme by cell sectorization in OFDMA based wireless networks**,” in *Fourth International Conference on Computer Sciences and Convergence Information Technology (ICCIT '09)*, pp. 800 –805, Nov. 2009.
- [10] A. Najjar, N. Hamdi, and A. Bouallegue, “**Efficient frequency reuse scheme for multi-cell OFDMA systems**,” in *IEEE Symposium on Computers and Communications (ISCC 2009)*, pp. 261 –265, July 2009.
- [11] P. Godlewski, M. Maqbool, M. Coupechoux, and J.-M. Kélif, “**Analytical evaluation of various frequency reuse schemes in cellular OFDMA networks**,” in *Proceedings of the 3rd International Conference on Performance Evaluation Methodologies and Tools*, ser. Value-Tools '08, pp. 1–32, 2008.
- [12] V. Jungnickel, M. Schellmann, L. Thiele, T. Wirth, T. Haustein, O. Koch, W. Zirwas, and E. Schulz, “**Interference-aware scheduling in the multiuser MIMO-OFDM downlink**,” *IEEE Communications Magazine*, vol. 47, no. 6, pp. 56 –66, June 2009.
- [13] M. Abaii, G. Auer, F. Bokhari, M. Bublin, E. Hardouin, O. Hrdlicka, G. Mange, M. Rahman, and P. Svac, “**IST-4-027756 WINNER II D4.7.2 v1.0 interference avoidance concepts**,” Wireless World Initiative New Radio (WINNER), Tech. Rep.

- [14] X. Zheng and B. Walke, “**Enhanced fractional frequency reuse to increase capacity of OFDMA systems**,” in *3rd International Conference on New Technologies, Mobility and Security (NTMS 2009)*, pp. 1–5, Dec. 2009.
- [15] M. Assaad, “**Optimal fractional frequency reuse (FFR) in multicellular OFDMA system**,” in *IEEE 68th Vehicular Technology Conference (VTC 2008-Fall)*, pp. 1–5, Sept. 2008.
- [16] B. Krasniqi, M. Wrulich, and C. Mecklenbrauker, “**Network-load dependent partial frequency reuse for LTE**,” in *9th International Symposium on Communications and Information Technology (ISCIT 2009)*, pp. 672–676, Sept. 2009.
- [17] Z. Xie and B. Walke, “**Performance analysis of reuse partitioning techniques in OFDMA based cellular radio networks**,” in *IEEE 17th International Conference on Telecommunications (ICT)*, pp. 272–279, April 2010.
- [18] C. E. Shannon, “**A mathematical theory of communication**,” *Bell Systems Technical Journal*, vol. 27, pp. 379–423, 623–656, 1948.
- [19] A. Molisch, **Wireless Communications**. Wiley, 2005.
- [20] V. Abhayawardhana, I. Wassell, D. Crosby, M. Sellars, and M. Brown, “**Comparison of empirical propagation path loss models for fixed wireless access systems**,” in *IEEE 61st Vehicular Technology Conference (VTC 2005-Spring)*, vol. 1, pp. 73–77, May 2005.
- [21] Electronic Communication Committee (ECC) within the European Conference of Postal and Telecommunications Administration (CEPT), “**The analysis of the coexistence of FWA cells in the 3.4 - 3.8 GHz band**,” Electronic Communication Committee (ECC), Tech. Rep. 33, May 2003. [Online]. Available: <http://www.erodocdb.dk/Docs/doc98/official/pdf/ECCREP033.PDF>

- [22] V. Erceg, K. V. S. Hari, M. Smith, and D. S. Baum, “**Channel models for fixed wireless applications,**” *Contribution to IEEE 802.16.3*, July 2001. [Online]. Available: <http://www.nari.ee.ethz.ch/commth/pubs/p/EHSB01>
- [23] COST Action 231, “**Digital mobile radio towards future generation systems, final report,**” European Communities, EUR, Tech. Rep. 18957, 1999. [Online]. Available: http://www.lx.it.pt/cost231/final_report.htm
- [24] S. Hamouda, S. Tabbane, and P. Godlewski, “**Improved reuse partitioning and power control for downlink multi-cell OFDMA systems,**” in *Proceedings of the 2006 workshop on Broadband wireless access for ubiquitous networking*, ser. BWAN '06, 2006.
- [25] S. Kiani and D. Gesbert, “**Optimal and distributed scheduling for multicell capacity maximization,**” *IEEE Transactions on Wireless Communications*, vol. 7, no. 1, pp. 288 –297, Jan. 2008.
- [26] Z. Wang and R. Stirling-Gallacher, “**Frequency reuse scheme for cellular OFDM systems,**” *Electronics Letters*, vol. 38, no. 8, pp. 387 –388, April 2002.
- [27] T. S. Rappaport, **Wireless Communications: Principles and Practice, 1st ed.** Piscataway, NJ, USA: IEEE Press, 1996.
- [28] S. S. Choi and D. H. Cho, “**Coordinated resource allocation scheme for forward link in sectorized CDMA systems,**” in *IEEE 56th Vehicular Technology Conference (VTC 2002)*, vol. 4, pp. 2356 – 2360, 2002.
- [29] L. Fang and X. Zhang, “**Optimal fractional frequency reuse in OFDMA based wireless networks,**” in *4th International Conference on Wireless Communications, Networking and Mobile Computing (WiCOM '08)*, pp. 1 –4, Oct. 2008.

- [30] F. Gil, A. Claro, J. Ferreira, C. Pardelinha, and L. Correia, “**A 3-D extrapolation model for base station antennas’ radiation patterns,**” in *IEEE 50th Vehicular Technology Conference (VTC 1999)*, vol. 3, pp. 1341 –1345, 1999.
- [31] L. Thiele, T. Wirth, K. Börner, M. Olbrich, V. Jungnickel, J. Rumold, and S. Fritze, “**Modeling of 3-D field patterns of downtilted antennas and their impact on cellular systems,**” in *International ITG Workshop on Smart Antennas (WSA 2009)*, Berlin, Germany, Feb. 2009.